Icarus **152**, 151–171 (2001)
doi:10.1006/icar.2001.6619, available online at http://www.idealibrary.com on IDEAL®

Spectroscopic Evidence for High-Altitude Aurora at Jupiter from Galileo Extreme Ultraviolet Spectrometer and Hopkins Ultraviolet Telescope Observations

Joseph M. Ajello

Jet Propulsion Laboratory, California Institute of Technology, Pasadena, California 91109
E-mail: jajello@pop.jpl.nasa.gov

Donald E. Shemansky

University of Southern California, Los Angeles, California 90089

Wayne R. Pryor, A. Ian Stewart, and Karen E. Simmons

Laboratory for Atmospheric and Space Physics, University of Colorado, Boulder, Colorado 80303

Tariq Majeed, J. Hunter Waite, and G. Randy Gladstone

Southwest Research Institute, San Antonio, Texas 78228

and

Denis Grodent

Laboratoire de Physique Atmospherique et Planetaire, Universite de Liege, Liege, Belgium

Received March 31, 2000; revised December 21, 2000

The Galileo Extreme Ultraviolet Spectrometer (EUVS) and the Hopkins Ultraviolet Telescope (HUT) acquired UV spectra of Jupiter Aurora in the period from 1995 through 1997. The EUVS spectra spanned the wavelength range 540–1280 Å and the HUT spectra measured the extreme ultraviolet and far ultraviolet (EUV + FUV) wavelength range 830–1850 Å. Both sets of spectra present evidence of high-altitude, optically thin H_2 band emissions from the exobase region. The analysis of the UV spectra with a two-stream electron transport model and a jovian model auroral atmosphere indicates that the primary electron flux is composed of both soft and hard electrons with characteristic energies in the soft electron energy range of 20–200 eV and the hard electron range of 5–100 keV. The soft electron flux causes enhanced EUV emission intensities below 1100 Å. The soft electron flux may explain the high temperature of the upper atmosphere above the homopause as measured from H_3^+ rovibrational temperatures in the IR. For the deep aurora, a high primary characteristic energy above 5 keV is known to be present. The Galileo Energetic Particle Detector (EPD) has measured the electron distribution functions for energies above 15 keV in the middle magnetosphere. The high-energy distribution functions can be modeled by a combination of Maxwellian and kappa distributions. However, the EUV (800–1200 Å) portion of the HUT spectrum cannot be modeled with a single distribution of hard electrons as was possible in the past for the FUV (1200–1650 Å) spectrum measured by itself. The combination of EUV and FUV spectral observations by HUT serves to identify the amount of soft electron flux relative to the hard primary flux required to produce the high-altitude aurora in the neighborhood of the exobase.

Key Words: **Jupiter; aurorae; spectroscopy.**

INTRODUCTION

Recent studies of the charged particle environment in the Jupiter magnetosphere by the Galileo Energetic Particle Detector (EPD) (Mauk *et al.* 1996, 1999, Williams *et al.* 1999) and the Galileo Plasma instrument (PLS) (Frank and Patterson 2000) have served to characterize the behavior of particle sources for Jupiter's aurora. EPD has measured the distribution of high-energy charged particles (electrons, ions) from 15 keV to about 1 MeV over the period of the Galileo Prime Mission in 1996 and 1997. The distributions are found to be highly variable in space and time. Powerful jovian injection substorm events can occur at any longitude and local time, but they favor a radial distance of $\sim$12 R_j with a time scale of five minutes to a few hours. The characteristic primary electron energy, E_o, can change during this period from 30 to 100 keV. The electron distribution

0019-1035/01 $35.00

functions based on the Galileo EPD observations in the 10–20 R_j region of the middle magnetosphere can be modeled by a κ-distribution (power law for high energy electrons) with an isotropic pitch angle distribution. During Jupiter orbit insertion (JOI) PLS measured a large flux of 100 eV–2 keV low energy electrons. The electrons formed a field aligned current with particle motions taking place up and down field lines. Electron energy fluxes observed for radial distances beyond 5.9 R_j are capable of depositing 9 to 560 ergs/cm^2/s into the Jupiter ionosphere. The low energy flux is found to increase with decreasing energy. This type of electron flux distribution function can be modeled by a power law or an exponential function of energy (Strickland *et al*. 1993, Tsurutani *et al.* 1997). Both distributions, a high-energy and a low-energy, are probably effective in producing the aurora. Electron acceleration may take place in inverted-V structures when field-aligned currents exceed critical values (Newell *et al*. 1991). However, the altitude for peak emission is quite different for these two types of aurora. Over the wavelength range of the Galileo Extreme Ultraviolet Spectrometer (EUVS), the column-integrated emerging H Lyman series and H_2 Rydberg band spectrum is produced over a wide range of altitudes by both distributions. The EUV resonance band spectrum (transitions ending in $v'' = 0$) between 800 and 1100 Å is severely attenuated below 2000 km altitude (altitudes are referenced to the 1 bar level) in the exobase region by column densities of H_2 exceeding 10^{15} cm^{-2}. Deeper in the atmosphere vibrational bands of H_2 with $v'' = 1$ can also be trapped. The bands ending in $v'' = 1$ escape the jovian atmosphere with large intensity, only if produced above the homopause high in the atmosphere at an altitude above 400 km (Ajello *et al*. 1998, Wolven and Feldman 1998). The penetration to different column densities of H_2 by a combined soft and hard electron distribution will produce a highly variable combined EUV and FUV spectrum.

A two-stream electron transport model, recently developed by Grodent *et al*. (2000), is used in the analysis of the Galileo and HUT data presented here. Grodent *et al*. (2000) have synthesized the multispectral vertical structure information to place constraints on the equilibrium atmosphere produced by the auroral heating, an identical approach to the thermal model chosen here. The constraints in the model arise from a host of recent remote sensing and *in situ* observations. The *in situ* observations were already mentioned. Remote sensing images in the UV (Prange *et al*. 1997, 1998, Clarke *et al*. 1998), visible (Ingersoll *et al*. 1998, Vasavada *et al*. 1999) and IR (Drossart *et al*. 1993, Kim *et al*. 1998) aurora made with high spatial resolution cameras reveal the morphological details of the connection between the planet's magnetosphere and upper atmosphere in the auroral oval region. The mean dimensions of the main aurora oval are found from the Galileo solid state imaging (SSI) observations (Vasavada *et al*. 1999) to exhibit the following characteristics: (1) a vertical extent of 120 ± 30 km with a maximum intensity at 245 ± 30 km above the limb and (2) a horizontal width that varies from 170–1000 km (narrowest in the form of a thin arc near local dawn when the Galileo Ultraviolet Spectrometer (UVS) and EUVS obtain most spectra). The vertical temperature structure is determined by constraints levied by the following findings: (1) hydrocarbon thermal IR profiles of 150–400 K in the 0.1 mb ($\sim$170 km) to 1 μb range (the latter pressure corresponds to a range from 280 km in the nonauroral polar atmosphere to 380 km in the auroral polar atmosphere) from Voyager IR spectra (Drossart *et al*. 1993), (2) H_2 FUV thermal line profiles taken from high-resolution Hubble Space Telescope (HST) observations of Lyman and Werner band rotational lines yield temperatures of 400–850 K (270–650 km) (Liu and Dalgarno 1996, Trafton *et al*. 1994, 1998), which are weighted most heavily by emission at the peak of the hard electron deposition, and (3) near IR H_3^+ rotation–vibration overtone and fundamental bands which are modeled by a temperature of 700–1200 K define a pressure range between the 1 μbar and 0.1 nb level (400–2000 km) (Kim *et al*. 1998, Drossart *et al*. 1993, Lam *et al*. 1997, Perry *et al*. 1999).

The Galileo EUVS observations discussed here were obtained from 1996 to 1997 during the Prime Mission 11-orbit satellite tour G1-E11. The UV subsystem on the Galileo orbiter consists of two separate spectrometers (Hord *et al*. 1992). The EUVS measures radiation from 540–1280 Å and is on the spinning section of the spacecraft. The UVS is mounted on the scan platform and operates from 1130 to 4320 Å. The EUVS acquired aurora data from Jupiter as the slit aligned with the ecliptic plane drifted across the dawn terminator central meridian longitude during orbits G1 through E11. We have recently reported results on the EUVS and UVS observations of the Galileo aurora (Ajello *et al*. 1998, Pryor *et al*. 1998, 2000, James *et al*. 1998). In the only previous analysis of the Galileo EUVS observations we used a slab model (a layer of emitting gas overlaid with an absorbing gas) to fit the EUVS spectral data (Ajello *et al*. 1998). Many improvements to the initial approach are considered here. First, we use a two-stream electron transport code coupled to a one-dimensional thermal and composition structure code to determine the altitude of Jupiter's auroral atmosphere (Grodent *et al*. 2000). The atmosphere is divided into 200 layers of vertical extent 5–20 km from 0–4000 km altitude. The emission emerging at the top of the atmosphere from every layer is added together to form a model emission spectrum. Model line spectra are generated for molecular hydrogen for the thermodynamic conditions at each layer. Within each layer a model line spectrum is produced from each differential electron flux element in the secondary electron spectrum (really a combined degraded primary + secondary electron distribution) from the 11 eV threshold for the Lyman bands to very high electron impact energy ($\sim$500 keV). These 70 energy-dependent spectra at each altitude are summed to give the emission from each layer. Self-absorption and hydrocarbon absorption from the heated model auroral atmosphere determine the attenuation in the UV spectrum from each layer. The emerging line spectrum is convolved with the instrument line spread function. The model is compared with the spectral observations for the north composite spectrum (sum of G1 to E11 north spectra) and for the south composite spectrum to

determine the average energy input, Q_o, to the aurora. The EUVS spectrum is not sensitive to E_o, the most probable energy from the high-energy component of the auroral flux. The lack of sensitivity arises from the fact that the EUVS spectrum is produced high above the deposition peak in the auroral atmosphere.

The HUT observation of the Jupiter north polar region occurred on March 9, 1995, near local noon and over the central meridian longitude of 186–203° and lasted approximately $\frac{1}{2}$ hour (Wolven and Feldman 1998). The observation of the auroral oval underfilled the HUT slit ($10'' \times 56''$), which was oriented parallel to the equator. Morrissey *et al*. (1997) estimated the angular size of the auroral region from a set of simultaneous HST wide field planetary camera (WFPC 2) images, to be 4.5×10^{-10} sr. It appears that the entire oval and polar cap regions were visible at the time of observation. The observation occurred at an Earth–Jupiter distance of 5.2 AU. The HUT instrument, part of the Astro-2 observatory on the Space Shuttle Endeavor Mission, is described in detail elsewhere (Kruk *et al*. 1995). The HUT observations were spectrally unique, since the EUV and FUV wavelength regions were measured at ten times higher resolution than the Galileo EUVS (3.0 Å vs 30 Å full-width-half-maximum (FWHM)). This set of data will be shown to constrain both E_o and Q_o at the time of the observation. In addition to the previously reported hard electron flux of 5–100 keV (Dols *et al*. 2000, Trafton *et al*. 1994, 1998, Kim *et al*. 1995, 1997, Gladstone and Skinner, 1989, Ajello *et al*. 1998), we use the HUT spectrum to show that a high-altitude soft-electron primary beam is needed to model the EUV emissions. This HUT data set was previously modeled with a single-layer slab model (Wolven and Feldman 1998). We present here our analysis of the HUT spectrum with an auroral atmosphere that is constructed on the basis of auroral heating. The Grodent *et al*. (2000) model of the auroral atmosphere includes chemical heating and cooling based on a two-stream electron energy deposition code and the heat conduction equation. A multilayered atmosphere distributed by thermal pressure balance and eddy diffusion leads to a more physically significant description of the auroral source. The previous slab model of Wolven and Feldman (1998) did show that the intensities from the Werner (v', $v'' = 1$ and 2) progressions from HUT were weaker than the intensity from the model. The upper atmosphere suprathermal enhancement of population $v'' = 1$ and 2 and higher levels in the aurora is expected from lifetime considerations of vibrational transitions (Cravens *et al*. 1975, Cravens 1987). Vibrationally excited H_2 is created in copious quantities by slow electron collisions on ground state $v'' = 0$ molecules and by Rydberg state emissions and other processes (Cravens 1987, Majeed *et al*. 1991). Cravens (1987) has shown that the vibrational temperatures of all levels are enhanced above the neutral gas temperature in the aurora. In the region of maximum deposition for the hard electrons the relative population of the $v' = 1$ and 2 levels corresponds to a vibrational temperature of about twice the gas temperature.

In this paper we analyze and compare two Jupiter auroral data sets—the Galileo EUVS Prime Mission spectra and the HUT ultraviolet spectra from the Astro-2 mission. The data sets show similar EUV relative intensity spectral characteristics. The best fit to the spectral intensity is achieved by including two auroral primary distribution functions. The dominant hard electron flux (5–100 keV) deposits a great deal of energy in the vicinity of the homopause. The emerging emission at the top of the atmosphere, produced near the homopause region, is greatly weakened by self-absorption. EUV spectra from the stratosphere are completely eliminated by self-absorption and by hydrocarbon absorption. The intensity of bands ending on $v'' = 0$ and 1 is redistributed to longer wavelength bands in the FUV radiating to higher vibrational levels of the ground state. The additional energy input of very soft electrons (~100 eV) serves to heat the exobase through dissociative processes and excite the Rydberg bands of H_2. The excited molecules radiate a nearly optically thin spectrum, similar in intensity structure to an optically thin electron-excited spectrum of $e + H_2$ measured in the laboratory (Jonin *et al*. 2000, Liu *et al*. 2000). The best-fit models of the observations estimate E_o, the characteristic energy, and Q_o, the incident energy flux—the two salient auroral characteristics (Strickland *et al*. 1993). We then compare the results of the HUT and Galileo observations to results from a laboratory data set. Based on the requirements of a low-electron-energy heat source for the exobase and a high-electron-energy heat source for the deep aurora penetration we make a case for the importance of assembling a multicomponent primary electron distribution function. The distribution may provide the distribution of primary electrons needed to drive the aurora. This extended primary energy distribution function (10 eV to 100 keV) in the auroral zone could also be the manifestation of the same type of intense low-energy electron beams observed *in situ* by the Galileo PLS (Frank and Patterson 2000). A measured low-energy electron distribution can be modified in the inner magnetosphere by field-aligned electric fields to produce the deep aurora.

THE GALILEO EUVS OBSERVATIONS

We show the north and south composite EUVS spectra in Fig. 1. The EUVS successfully acquired signal from the aurora on orbits G1, C3, E4, E6, G7 (south only), C9, and E11 (north only). Figure 1a shows the observations as a count rate, which will be compared to a model to give absolute source fluxes. Figure 1b shows the total counts achieved over the two-year mission. The composite spectrum consists of 69 s worth of data in the north and 74 s in the south. The low integration time is a consequence of the fact that the EUVS boresight spins through the sky with low duty cycle on the aurora. The north and south spectra are seen to be identical to within 10%. The torus spectrum has been previously shown to be weak (maximum count rate of 0.5 c/s/channel at 680 Å). Since each observation contains both the aurora and the torus, the torus background spectrum in Ajello *et al*. (1998) has been subtracted from these spectra. We plot the 1σ statistical error bars for every tenth wavelength element. We use the fact that there are on average 2.5 photoelectrons

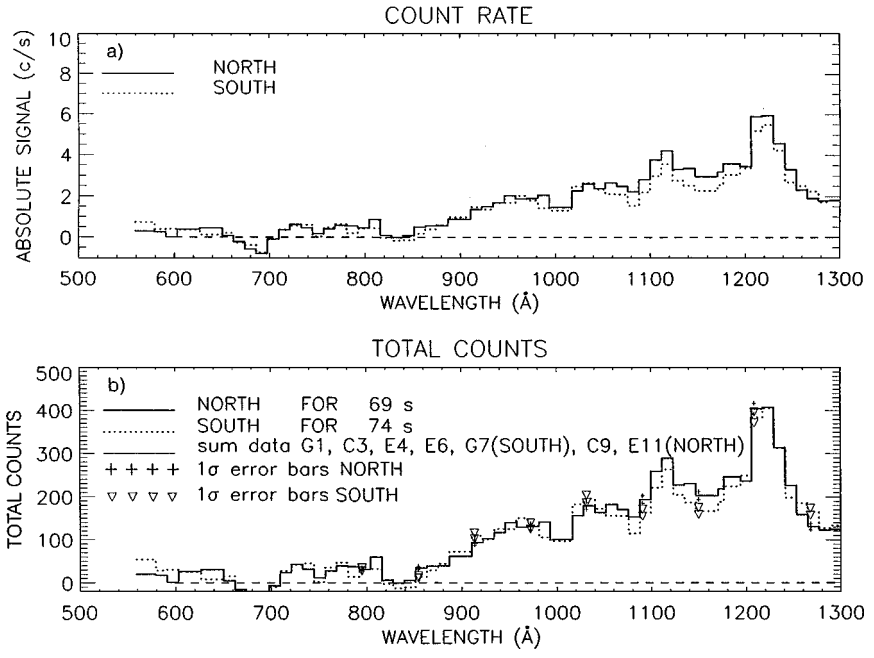

FIG. 1. The EUVS north and south composite spectra: (a) the composite spectra as a count rate from 500–1300 Å, (b) the composite spectra total counts from 500–1300 Å. The 1 σ error bars are shown every 20 channels as (+) signs for the north and triangles for the south. The dashes are an estimated background level.

produced per detected photon. The photon statistics are better than 10% throughout the spectrum. The times of the individual observations are given in Table I. Six of the eleven orbits yielded measurable signals on each pole. We show the individual spectra on a per orbit basis in Fig. 2 for the northern aurora and in Fig. 3 for the southern aurora. All of the observations were of the dawn meridian of the planet (incoming trajectory) except for the C9 observation of the dusk sector (outgoing trajectory). The estimated filling factor based on a 200-km wide auroral oval is given in Table I along with the distances from the spacecraft to Jupiter and the cosines of the emission angle, both at the center of the observation time. The brightest observed aurora in terms of spectral irradiance at the spacecraft in the H_2 Rydberg bands occurred in the north on E11 and in the south on G7. The spacecraft was the closest to Jupiter for these observations, about 20 R_j. Adding a $1/R_j^2$ correction factor for an underfilled field-of-view indicates all the EUV intensities were within 50% of one another. The composite spectra given in Fig. 1 are based on the sum of the counts of the individual orbital spectra divided by the total observation time.

On each orbit the EUVS sampled simultaneously both the main aurora oval and the diffuse polar cap aurora. The main oval has persistent bright features that can vary in brightness on a long time scale as noted by Prange *et al.* (1998). Globally averaged variations of a factor of two can be expected over periods of a year or more. The diffuse emissions poleward of the oval also have brightnesses that vary in an image from the limit of detection to being nearly as bright as the main oval (Clarke *et al.* 1996). We see large long-term temporal variations in the averaged north and south aurorae with the Galileo EUVS spectra. Thus, the summed north and south EUVS spectra of Table I presented in Fig. 1 are a low-wavelength-resolution record of the "average" EUV aurora on Jupiter over 1996–1997.

We describe the instrument performance based on the accumulated Very Local Interstellar Medium (VLISM) cruise observations of He(584 Å) and H Ly α. The observation of the VLISM for over 10^6 s during the Earth One encounter in 1990 by the Galileo EUVS offered an opportunity to provide an in-flight calibration of the instrument transmission function (see Appendix).

The instrument operation has been described previously (Ajello *et al.* 1998). In brief, the EUVS duty cycle for observing the north or south aurora during a complete rotation can be calculated as the 0.17° field-of-view (FOV) divided by 360° of rotation angle to equal 4.7×10^{-4}. This duty cycle is equivalent to an aurora observing time of 1 s for every 30 min of observing time in the spin–scan mode of operation. Nominally there is about 10 s of accumulated photon counts on each of the seven orbits spaced over two years. Actual observation duration times varied from 4–22 s. Thus the G1 north observation time of 12.1 s was obtained from 6 h of observations on the H_2 Rydberg band aurora. The observation times given in Table I show a small modification from the times given in Ajello *et al.* (1998) for the "Big Four" aurora set of orbits G1–E4. The timing of the observations depended on the orbital period and the orientation of the spacecraft spin axis, since the $0.17 \times 0.86°$ FOV EUVS is mounted on the spinning rotor section of the spacecraft. Twenty-four spatial sectors define the area observed during each spacecraft spin. EUVS measured the Jupiter/torus system usually on the inbound side of Jupiter periapsis. We list

TABLE I
The Galileo EUVS Aurora Observations 1996–1997

Orbit	Location	Latitude/ longitude (mid-time)	μ Cosine Emission angle (mid-time)	Fill factor (%) for 200-km wide auroral source	Spececraft distance (R_J)	Day-of-Year/ observation start time	Day-of-Year/ observation end time	Spacecraft clock start time (RIMS)	Spacecraft clock end time (RIMS)	Observation time (seconds)	Record (flush number from zero)	Sector # (from zero north)
G1	NORTH	58–70N, 150–220W	.24	.77	67.6	96–172/18^h52^m	96–173/02^h07^m	3488375	3488806	12.1	31–39 of 101	14
G1	SOUTH	76–84S, 120–270W	.17	.53	67.6	96–172/17^h51^m	96–173/03^h08^m	3488315	3488866	15.5	30–40 of 101	17, 18
C3	NORTH	65–77N, 60–120W	.35	.40	61.7	96–304/08^h08^m	96–304/13^h41^m	3675730	3676059	9.3	41–47 of 90	9
C3	SOUTH	70–73S, 331–60W	.30	.68	62.8	96–304/04^h16^m	96–304/15^h42^m	3675500	3676179	19.	37–49 of 90	13, 14
E4	NORTH	54–74N, 100–210W	.47	1.02	55.2	96–347/17^h21^m	96–348/06^h33^m	3737516	3738300	22.0	43–57 of 109	11
E4	SOUTH	77S, 308W	.33	1.02	54.0	96–347/19^h25^m	96–348/04^h32^m	3737639	3738180	15.2	45–55 of 109	15, 16
E6	NORTH	66N, 310–360W	.22	3.3	28.8	97–049/10^h42^m	97–049/14^h46^m	3833966	3834207	6.8	12–15 of 19	9, 10
E6	SOUTH	68S, 10–330W	.26	3.3	28.8	97–049/10^h42^m	97–049/14^h46^m	3833966	3834207	6.8	12–15 of 19	18, 19
G7	SOUTH	65S, 100–30W	.36	3.8	24.7	97–092/14^h44^m	97–092/17^h20^m	3895444	3895599	3.0	24, 25 of 30	15, 16
C9	NORTH	69N, 130–90W	.23	4.8	19.8	97–179/16^h06^m	97–180/00^h40^m	4019429	4019937	14.3	0–4 of 25	19–21
C9	SOUTH	66–72S, 130–60W	.31	4.8	19.8	97–179/16^h06^m	97–180/00^h40^m	4019429	4019937	14.3	0–4 of 25	7, 8
E11	NORTH	60–70N, 240–180W	.19	4.4	21.4	97–309/11^h27^m	97–309/13^h58^m	4204296	4204445	4.2	24–27 of 37	7, 8

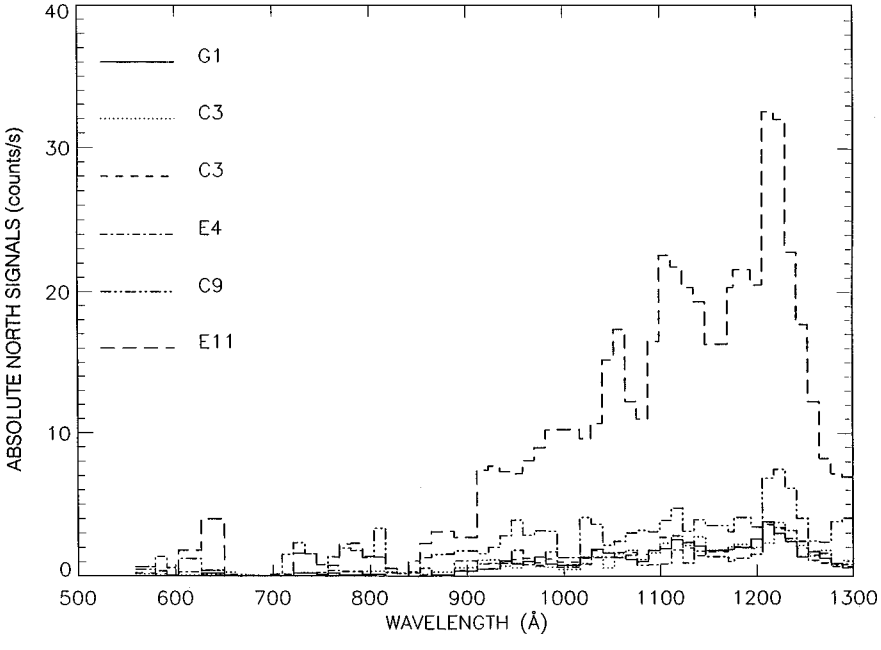

FIG. 2. The absolute spectral count rates for the six orbits on which the Galileo EUVS observed the northern aurora.

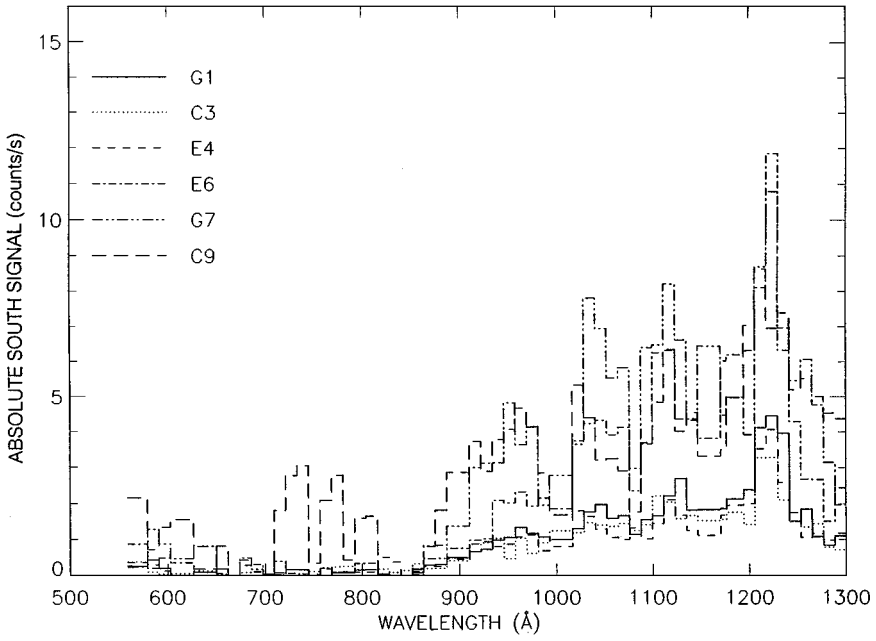

FIG. 3. The absolute spectral count rates for the six orbits on which the Galileo EUVS observed the southern aurora.

the aurora/torus data record numbers measured (see Ajello *et al*. 1998) with respect to record zero beginning at -9 R_j (Europa orbit) with respect to Jupiter center and continuing to $+9$ R_j on the other side of the orbit. The sector numbers within each record containing measurable H_2 band auroral emission are also listed. The other record numbers contain exclusively torus, H Ly α dayglow, and/or sky background signal. Extreme intervals ranging from 43 days elapsed time (C3 and E4) to 130 days elapsed time (G1–C3 and C9–E11) occurred between orbit observations.

THE MODEL

To our knowledge there has been no previous analysis of Jupiter aurora EUV spectra involving a multilayer model auroral atmosphere. Previous analysis included a thin-slab single layer (Wolven and Feldman 1998) and a three-layer model (Ajello *et al*. 1998). Slab models lead to an average fit that reflects the average atmosphere composition, weighted by percentage of outgoing emission emanating from a given region. However, given the fact that the atmosphere is not homogeneous, a slab model does not yield or make use of the atmospheric weighting function. In our work, similar to the work of Dols *et al*. (2000) and Pryor *et al*. (2000) in the FUV, the atmospheric composition and primary electron degradation is explicitly considered. Each atmospheric layer contributes to the emerging spectrum by virtue of the interaction of the local secondary electron (plus primary) spectrum with the local H_2 density. We choose to use the same approach to model the EUV spectra as Grodent *et al*. (2000) have prescribed for the analysis of HST FUV spectra. Our model is a synthesis of (1) the spectral line H_2 Rydberg code for electron impact described by Shemansky (1985) and Ajello *et al*. (1984, 1988, 1998), (2) the two-stream electron energy degradation transport code derived by Waite *et al*. (1983, 1988), and (3) the one-dimensional heat conduction, which includes the heating of the atmosphere by the auroral electron precipitation (Grodent *et al*. 2000). Grodent *et al*. (2000) recognized that the thermal constraints placed on the upper atmosphere by the H_3^+ rovibrational temperatures required soft electron impact with an E_o of $\sim$1 keV to achieve the exospheric temperatures of 700–1300 K. We will show that an even softer electron flux of E_o of about 0.1 keV is needed to explain the EUV spectrum. Grodent *et al*. (2000) do not consider heating of the upper atmosphere by protons or ions due to the nondetection of OII or SII lines in the UV. The ion aurora are observed in the X-ray region which occur deeper in the atmosphere (Bhardwaj and Gladstone 2000).

As a starting point we describe the emerging spectrum seen at either the Galileo or HUT spacecraft resulting from an incoming distribution of electrons. The emerging integrated intensity at any wavelength is given by

$$4\pi\, I_\lambda(R) = 10^{-6} \int_0^\infty V_\lambda(z) \exp(-\tau_\lambda/\mu)\, dz/\mu, \qquad (1)$$

where $4\pi\, I_\lambda(R)$ is the total slant surface brightness in Rayleighs (1 R is a unit of 10^6 photons/cm^2/s into 4π steradians) at the top of the atmosphere at wavelength λ. $V_\lambda(z)$ is the volume emission rate at any altitude z measured with respect to the bar surface level. μ is the cosine of the emission angle. τ_λ is the vertical optical thickness at wavelength λ between the atmospheric layer at altitude z and the top of the atmosphere due to the sum of effects of self-absorption and hydrocarbon absorption (Ajello *et al*. 1998).

The volume emission rate, $V_\lambda(z)$ from a spectral line at wavelength λ, can be written as

$$V_\lambda(z) = g_l(z)\,\omega_{lm}(\lambda)(1-\eta_l), \quad (2)$$

where $g_1(z)$ is the excitation rate (excitations per unit volume per second) at altitude z into an upper state characterized by quantum numbers α, v′, and J′ for the upper electronic state principal quantum number, the vibrational level quantum number, and the rotational level quantum number, respectively, and denoted by index l. The index m refers to the quantum numbers β, v″, and J″ for the lower electronic, vibrational, and rotational quantum numbers, respectively. $\omega_{lm}(\lambda)$ is the emission branching ratio for the transition $l \rightarrow m$ at wavelength λ and is given by

$$\omega_{lm}(\lambda) = A_{lm}/A_l, \quad (3)$$

where A_{lm} is the Einstein spontaneous transition probability from the upper state to a lower state with index m, and A_1 is the total emission transition probability to all lower states. The emission branching ratios for the four Rydberg states ($B^1\Sigma_u^+$, $B'^1\Sigma_u^+$, $C^1\Pi_u$, and $D^1\Pi_u$) observed in the EUV spectra are considered in the model. The factor η_1 is the nonradiative yield of predissociation and preionization for the upper state, l (Jonin *et al*. 2000, Liu *et al*. 2000). The model at the present time does not consider the conservative nature of the self-absorption process, and as a consequence the model necessarily underestimates the fluorescent emission intensities to $v'' > 1$ vibrational for both the Lyman and Werner bands. This effect may lead to overestimates of auroral energy by ~20% (Wolven and Feldman 1998). However, there is no detectable change in the relative intensities of long wavelength FUV spectra (1100–1650 Å) of electron-excited H_2 obtained in the laboratory at foreground abundances of 10^{15} cm^{-2} from laboratory experiments similar to Jonin *et al*. (2000).

The excitation rate, $g_1(z)$, is proportional to the total number of molecules in the initial ground state level, the electron flux, and the excitation cross section. The excitation rate is given by

$$g_1(z) = N(z, T)\int F(\varepsilon, z)\left[\sum_X f_X(T)\,Q_{lX}(\varepsilon)\right]d\varepsilon, \quad (4)$$

where N(z, T) is the atmospheric H_2 density at altitude z with a local kinetic temperature T, and f_X is the fraction of the H_2 molecules in the initial ground vibrational level v_i and rotational level J_i (see notation of Ajello *et al*. 1998). The sum extends over the fine structure rotational branches for Σ and Π transitions. $F(\varepsilon, z)$ is the electron distribution function in flux units at energy ε and altitude z, $Q_{lX}(\varepsilon)$ is the fine structure excitation cross section for a rotational line (or continuum transition) $X \rightarrow l$ for an electron impact collision of energy ε given by Liu *et al*. (1998). The emission cross sections for all Rydberg states and EF $^1\Sigma_g^+$ valence states have been recently remeasured by Jonin *et al*. (2000), Liu *et al*. (1998, 2000), and Dziczek *et al*. (2000). The EF, GK, and H states produce cascade excitation to all vibrational levels of the B state. The emission cross sections, excitation cross sections, and predissociation yields found in these recent references represent substantial changes from earlier estimates (Ajello *et al*. 1988, Shemanksy *et al*. 1985).

The double integral computer model for the emergent EUV spectrum represented by Eq. (1) combined with Eq. (4) was allowed to sample a wide range of auroral conditions. Two neutral atmosphere models were studied. First, the north equatorial belt (NEB) model of Gladstone *et al*. (1996) was considered. The NEB photochemical model distributions of H_2, H, He, CH_4, C_2H_2, and other minor hydrocarbon species were calculated by Gladstone *et al*. (1996). The densities of the NEB model have been scaled to the Galileo Probe results of Seiff *et al*. (1998) by adopting the local effective gravity at 60°N. This gravitational change converts the NEB model to a polar model. The reference altitude was chosen to be the 1 bar level at 60°N where the effective acceleration of gravity has increased relative to the local gravity at the probe descent location near the equator. We call this polar model the initial atmosphere model for the two-stream electron energy deposition code. The modeled exospheric temperature is 940 K, based on H_3^+ IR spectra (Dols *et al*. 2000). By way of altitude reference, Vasavada *et al*. (1999) have shown that the auroral primary electron flux penetrates to the 245-km altitude at a polar model pressure of 4 μb. The altitude attained corresponds to an H_2 column density of 3.9×10^{20} cm^{-2}. It has been shown that the primary electron flux requires a characteristic energy of 25 keV for penetration (Dols *et al*. 2000). The auroral electrons heat the atmosphere and modify the temperature. The output of the coupled two-stream thermal structure code produces the final atmosphere to be used in modeling the volume emission rate given by Eq. (2). The diffusive equilibrium model atmosphere code for the final auroral atmosphere gas distribution and the heat conduction equations for the new temperature profile used in the model in Eq. (2) have been described by Grodent *et al*. (2000).

We have considered a wide range of incoming electron flux distribution functions. Using a basic model consisting of a summed kappa distribution function plus a Maxwellian we have varied the primary characteristic energy, E_{max} ($2\,E_{max}$ is the mean energy in the electron distribution function), of the Maxwellian from 1 keV to 100 keV. The selected kappa (κ) distribution has a κ-spectral index of 2.1 and a characteristic energy, E_κ, of 15 keV. The electron energy distribution measurements from the EPD instrument, which is responsible for the κ-distributions employed in the two-stream electron transport models, have sensitivity to electrons from 15 keV to the MeV range. The function form is given by

$$\Phi = \Phi_{max} + \Phi_\kappa, \quad (5)$$

where

$$\Phi_{max} = AQ_{max}E/E_{max}^3\exp(-E/E_{max}), \quad (6)$$

and

$$\Phi_\kappa = BQ_\kappa E/E_\kappa[1 + E/\kappa E_\kappa]^{-\kappa-1}. \quad (7)$$

We began the modeling by assuming a Maxwellian energy flux $Q_{max} = 65$ ergs/cm^2/s and a κ-flux of $Q_\kappa = 20$ ergs/cm^2/s. The mean pitch angle is 45°. The final total energy input is given by

$$Q_{final} = \beta(Q_{max} + Q_\kappa). \quad (8)$$

The best-fit regression coefficient, β (near unity), is determined for each observation from fitting the absolute count rate of HUT and Galileo observations to a model of the data, once a fill factor is determined. The ratio of Maxwellian to κ-energy input is held constant. In addition, a 3-κ distribution is used for one of the models. It has a unique character with $E_\kappa = 15$ keV ($\kappa = 2.1$), 30 keV ($\kappa = 7$), and 600 eV ($\kappa = 7$), respectively, for each one of the κ-distributions of the sum. The final energy input is given by an expression similar to Eq. (8) with the individual κ-distributions in a fixed ratio determined by $Q_\kappa = 20$, 30, and 50 ergs/cm^2/s, respectively. We show the initial electron distribution functions for the 25-keV Maxwellian in Fig. 4a, and the 3-κ distribution distribution in Fig. 4b, along with the distributions at three altitudes in the aurora: 300 km (near the homopause), 800 km (in the thermosphere), and 3000 km (in the exosphere). The degradation of the primary electron flux with energy in the atmosphere has been described by Grodent *et al*. (2000). Note both initial distributions have the high energy 15-keV κ-tail measured by EPD (R. Thorne, personal communication, 2000). The 25-keV Maxwellian distribution masks the 15-keV κ-tail. A large number of low-energy secondary electrons are generated at all altitudes in the aurora as the primary electrons slow down. The cross section for ionization is the largest of the loss processes in the Bethe high-energy region. The newly created low-energy electrons rapidly react with H_2 ambient gas through excitation, further ionization, and dissociation (Cravens 1987, Gerard and Singh 1982). However the loss processes are rather inefficient at high altitudes, since the atmosphere is tenuous and explains the rapid buildup of low-energy electrons at 800 km and 3000 km altitude. By 300 km, near the peak in energy deposition to the atmosphere, the loss processes with the atmosphere are capable of rapidly depopulating all electrons with energies above 11 eV due to the increased atmospheric density.

We show the important characteristics for each of the two model atmospheres in Fig. 5 (the NEB polar model) and Fig. 6 (two-stream electron transport auroral model). In Fig. 5b we show the initial atmosphere for the major atmospheric components: H_2 and CH_4. In Fig. 6a the total electron flux is shown as a function of altitude for the cases of a 3-κ distribution and 25-keV incident Maxwellian summed with a 15-keV κ-distribution component. The functional forms have been described above.

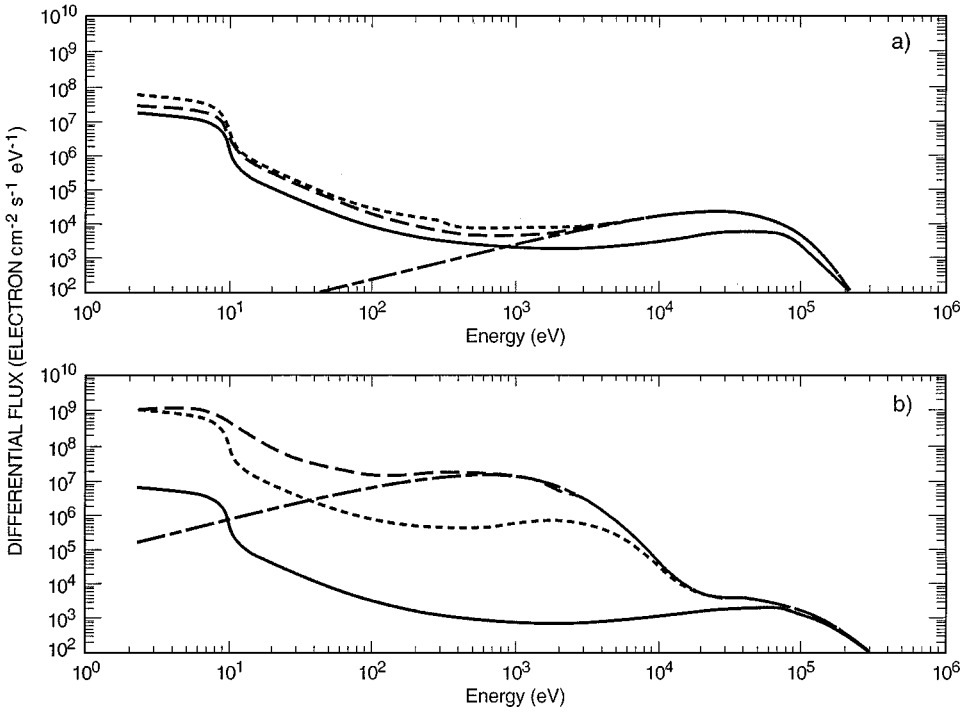

FIG. 4. (a) The differential flux of downward incoming primary electrons (dash–dot curve) at the top of the atmosphere along with the differential electron flux of upward plus downward electrons at 300 km (solid curve), 800 km (dotted curve), and 3000 km (dashed curve) for the 25 keV Maxwellian distribution. (b) The differential flux of downward incoming primary electrons (dash–dot curve) at the top of the atmosphere along with the differential electron flux of upward plus downward electrons at 300 km (solid curve), 800 km (dotted curve), and 3000 km (dashed curve) for the 3-κ distribution.

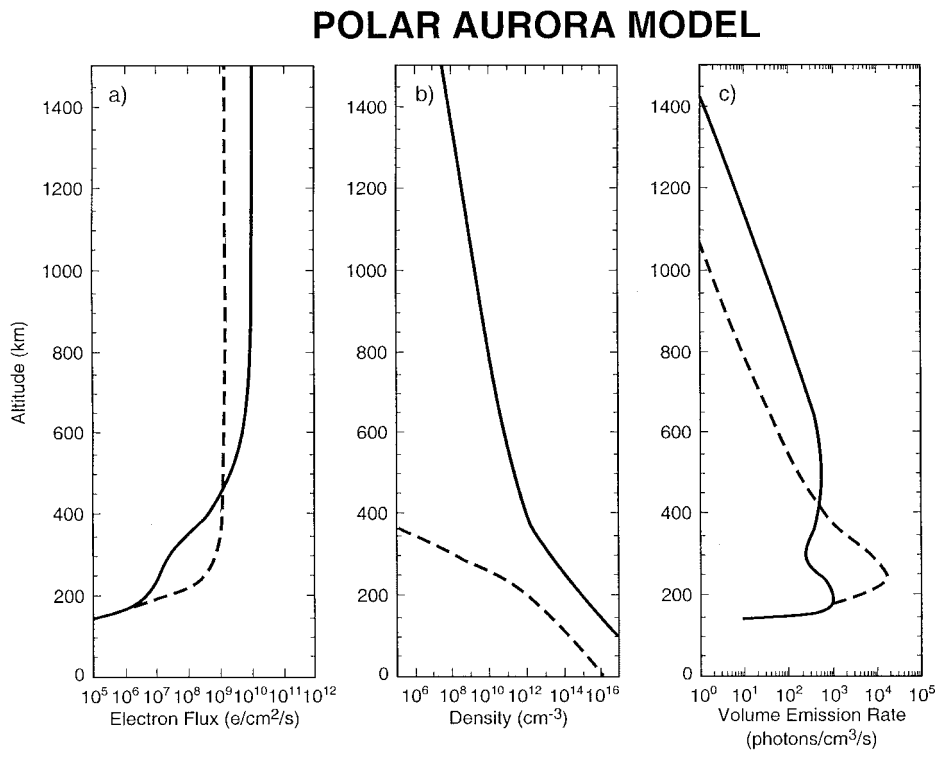

FIG. 5. The NEB polar model. (a) The total electron energy flux for the 25-keV Maxwellian distribution plus the 15-keV κ-distribution (dashed curve) and the 5-keV Maxwellian distribution plus the 15-keV κ-distribution (solid curve) shown as a function of altitude. (b) (Initial) atmosphere of H_2 density (solid curve) and CH_4 density (dashed curve) as a function of altitude. (c) The source function (volume emission rate) as a function of altitude is shown for the 25-keV Maxwellian (dashed curve) and the 5-keV Maxwellian (solid curve). Note the double peak in the volume emission rate from the high- and low-energy parts of the 5-keV Maxwellian distribution.

In Fig. 5a the total electron flux is also shown as a function of altitude for the cases of a 5-keV incident Maxwellian distribution summed with a 15-keV κ-distribution and a 25-keV incident Maxwellian distribution summed with a 15-keV κ-distribution. The altitude-dependent product of the electron flux (weighted with the emission cross section in Eq. (4) and the H_2 density is an important quantity reflecting the volume emission rate. In this regard the volume emission rate of Eq. (2) is shown in both Fig. 5c and Fig. 6c for only the EUV emissions (850–1200 Å) from the Rydberg band systems. The 25-keV Maxwellian electron flux penetrates to 300 km and is completely stopped by 150 km. A single peak in the volume emission rate is observed for Maxwellian characteristic energies from 15 keV to 50 keV, since the very high energy primary beam is composed of a Maxwellian and a κ-distribution, both distributions with similar mean energies. The peak in the volume emission rate for the 25-keV Maxwellian occurs very close to 250 km for both Fig. 5c and Fig. 6c. The profile for the volume emission rate for the 5-keV Maxwellian plus energetic κ-flux in Fig. 5c has two peaks. The 5-keV Maxwellian plus energetic κ-peak volume emission rate for the NEB polar atmosphere occurs at 480 km in Fig. 5. The 15-keV κ-component by itself has a peak volume emission rate near 190 km. The total electron flux for the 3-κ distribution shown in Fig. 6a has a predominant energy flux component of 600 eV. The low-energy 600-eV component is stopped before the homopause and a double peak in the EUV volume emission rate is found. The two peaks in Fig. 6c occur at 210 and 870 km, the former from the 15- and 30-keV κ-distribution and the latter from the 600-eV κ-distribution. Incident primary beam fluxes with characteristic energies below 5 keV will be stopped above the homopause as Fig. 6a indicates for the 600-eV κ-component and serve to heat the thermosphere. The smaller the primary energy for the incident primary flux, the higher the altitude location of the peak emission rate. At an intermediate incident primary energy of 10 keV (not shown) to a 5-keV and 25-keV primary flux the Maxwellian volume emission rate peak has decreased in altitude to 290 km and maintains the smaller 15-keV κ-distribution volume emission rate peak near 190 km. At 25-keV incident Maxwellian energy the two volume emission rate peaks from the 25-keV Maxwellian and the 15-keV κ-distribution merge near 250 km in both Fig. 6c and Fig. 6c. This column density of H_2 is near 5×10^{20} cm^{-2} in both the atmosphere model cases. The emission profile (FWHM) is broad, ~110 km (from 210 to 320 km) in Fig. 6c for the two-stream electron transport auroral model. This profile with a peak near 250 km seems to duplicate the description of the aurora visible profile from the SSI observations (Vasavada *et al.* 1999). For the NEB polar model the halfwidth is less, only 80 km. The other major difference is that the CH_4 column density has changed dramatically at this same altitude of 250 km with

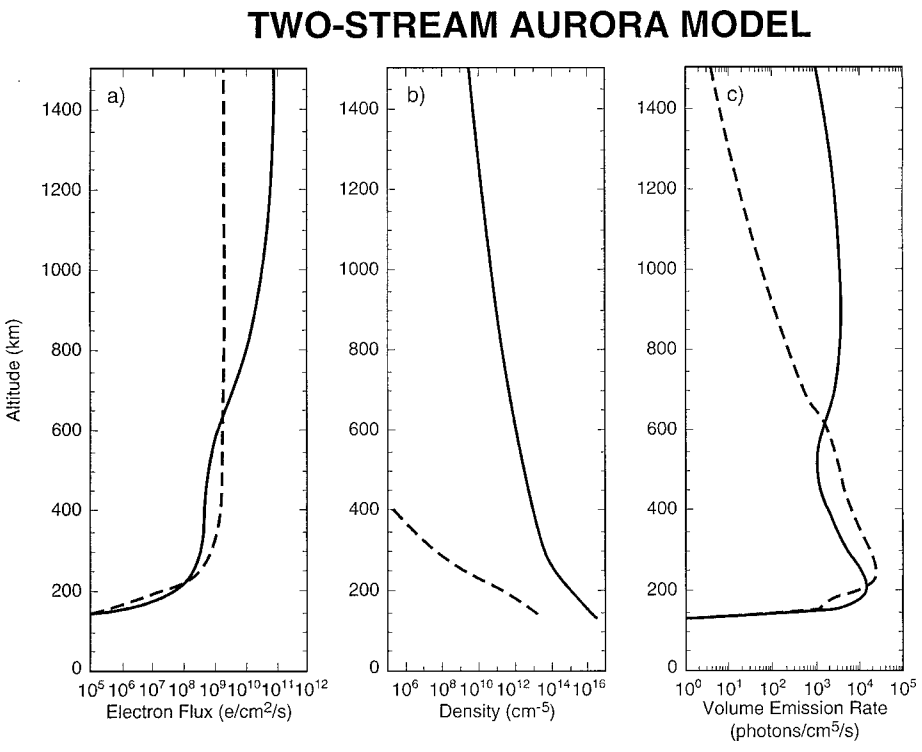

FIG. 6. The two-stream electron transport model. (a) The total electron energy flux for the 25-keV Maxwellian distribution plus the 15-keV κ-distribution (dashed curve) and the 3-κ distribution (solid curve) are shown as a function of altitude. (b) (Final) atmosphere of H_2 density (solid curve) and CH_4 density (dashed curve) as a function of altitude. (c) The source function as a function of altitude is shown for the 25-keV Maxwellian (dashed curve) and the 3-κ distribution (solid curve). Note the double peak in the volume emission rate from the high- and low-energy component functions of the 3-κ distribution.

values of 3.4×10^{16} cm^{-2} for the initial model (NEB polar model) versus 1.2×10^{15} cm^{-2} for the final model (two-stream aurora model). Thus, an analysis of an FUV spectrum by the two-stream electron transport aurora model atmosphere will require a higher primary energy to penetrate to the same hydrocarbon column density and match the same FUV color ratio (Livengood *et al*. 1990). The secondary plus primary 25-keV electron fluxes are shown in both Fig. 6 for the two-stream electron transport model as a function of altitude and Fig. 5 for the NEB polar model. The cooler exospheric temperature of the NEB polar model allows the primary beam to penetrate to a lower altitude. This is particularly obvious in the case of a 5-keV Maxwellian. The two exospheric temperatures differ, with values of 1340 K for the two-stream aurora model and 940 K for the NEB polar model. A comparison of the peak volume emission rates shows the peak volume emission rate has shifted upward in altitude from 480 km (see Fig. 5c) to 530 km (not shown). The two atmospheric models are similar below 250 km. However, at 400 km the two H_2 distributions are divergent by a factor of 10. The hotter two-stream thermal structure model allows the H_2 distribution to expand, producing 10 times the H_2 density at 400 km. The two-stream electron transport aurora model H_2 distribution density at 400 km is 9.6×10^{12} cm^{-3} with a local kinetic temperature of 577 K in contrast to the NEB polar model, which has a density of 9.6×10^{11} cm^{-3} and a temperature of 464 K (compare Fig. 5b and Fig. 6b).

Since we are dealing with the EUV (800–1200 Å) portion of the auroral UV spectrum, there is a large difference between the altitude location of the maximum in the volume emission rate and the altitude, or layer, producing the maximum in the emerging flux. The effects of both self-absorption and hydrocarbon absorption tend to move the altitude of the emission layer, which produces the maximum EUV signal measured at the spacecraft, far above the layer producing the maximum in the 'red' region of the FUV (near 1600 Å—see the next section for a definition of the 'red' region). The FUV 'red' region has no significant self-absorption or hydrocarbon absorption. The latter wavelength region tends to have the layer producing the maximum in the emerging flux signal at the identical altitude with the maximum in the volume emission rate in the UV. We show in Fig. 7 the plot of the count rate contribution to Galileo EUVS from the 3-κ and the 25-keV distributions for the two-stream aurora model. The maximum contribution to the signal in the EUV arises from the atmospheric layer at 273 km (FWHM = 130 km) at an H_2 column density of 4.6×10^{20} cm^{-2} for a 25-keV Maxwellian primary electron beam. The maximum signal contribution to the signal in the EUV occurs from the layer at 1040 km for the 3-κ distribution at an H_2 column density of 7×10^{17} cm^{-2} for the lower primary energy of 600 eV and 255 km for the two higher primary energies. The latter FWHM is exactly 100 km. It is clear that the 245 km altitude of the sharp visible emission peak observed by SSI (and necessarily

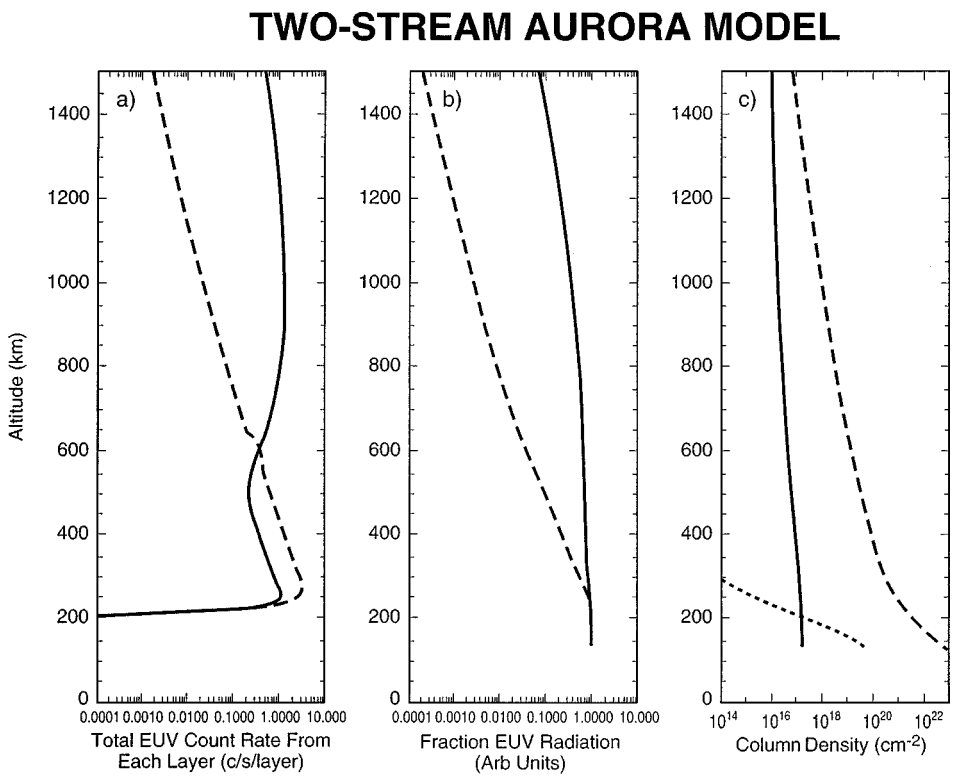

FIG. 7. The two-stream electron transport model. (a) The emerging spectrum EUV count rate produced at the EUVS from each of the 200 layers that are spaced every 5–20 km from 130–4800 km. The mean layer thickness is 10 km. The 25-keV Maxwellian count rate is shown (dashed curve) with the 3-κ distribution (solid curve). (b) The fractional running sum emission is shown as measured from the top-most layer for the 25-keV Maxwellian (dashed) and for the 3-κ distribution (solid curve). (c) The integrated column density of H (solid), H_2 (dashed curve), and CH_4 (dotted curve).

the 'red' region of the FUV [Clarke *et al.* 1998, Trafton *et al.* 1994, 1998, Liu and Dalgarno 1996]) could be explained by $\sim$25 keV characteristic energies for each of the Maxwellian + kappa distributions composing the primary beam. In addition, a softer primary energy component, with a characteristic energy between 1 keV and 5 keV, will produce a diffuse secondary emission high in the thermosphere. At incident energies below 600 eV a softer primary component will deposit its energy near the exobase. The exobase is located at approximately 2000 km above the 1 bar level for an exospheric temperature of 1340 K. The molecular H_2 density and atomic H density from the two-stream thermal structure model for these two hydrogenic species are the same within a factor of two at the exobase with a value close to 2×10^8 cm^{-3} and a foreground abundance of about 6×10^{15} cm^{-2}. The column distributions of H, CH_4, and H_2 aurora gases are plotted in Fig. 7. We will show that the EUV spectrum can only be fitted with an auroral model that has a contribution from very low-energy electrons below $\sim$200 eV.

To fully understand the importance of the EUV portion of the spectrum we show in Fig. 7 for both the 3-κ and the 25-keV Maxwellian cases the running sum of the fraction of the EUV radiation from 800–1200 Å from the top of the atmosphere that is collected by Galileo or by HUT. The altitudes where the bulk of the EUV radiation arises are dramatically different. The 3-κ distribution (solid line) has produced 75% of the total emerging intensity by integrating altitudes above 400 km, whereas the 25-keV Maxwellian plus energetic κ-distribution (solid) makes a 75% contribution for altitudes above 267 km. The 50% level for the 3-κ distribution is produced for altitudes above 827 km, while for the 25-keV Maxwellian the same level is reached at 300 km.

THE ANALYSIS OF THE HUT EUV OBSERVATIONS

The original goal of this paper was solely the evaluation of the Galileo EUVS composite north and south spectra shown in Fig. 1. We planned to analyze the observations with the model given in the previous section. We compared the data and model using a multiple linear regression analysis technique. The same general method of least squares was presented in Ajello *et al.* (1998) for the initial three-layer analysis of the Galileo UVS and EUVS observations. The simplest linear regression model, based on our knowledge of the source of the aurora emission, is composed of two independent physical vectors, which sum together to give the measured spectrum. The first spectral vector is composed of the H_2 Rydberg bands, which fill the 80 wavelength channels from 800–1250 Å (EUVS channels 41–120). The second spectral vector is the H Ly α auroral line. The best measure available for the Galileo EUVS slit function behavior at

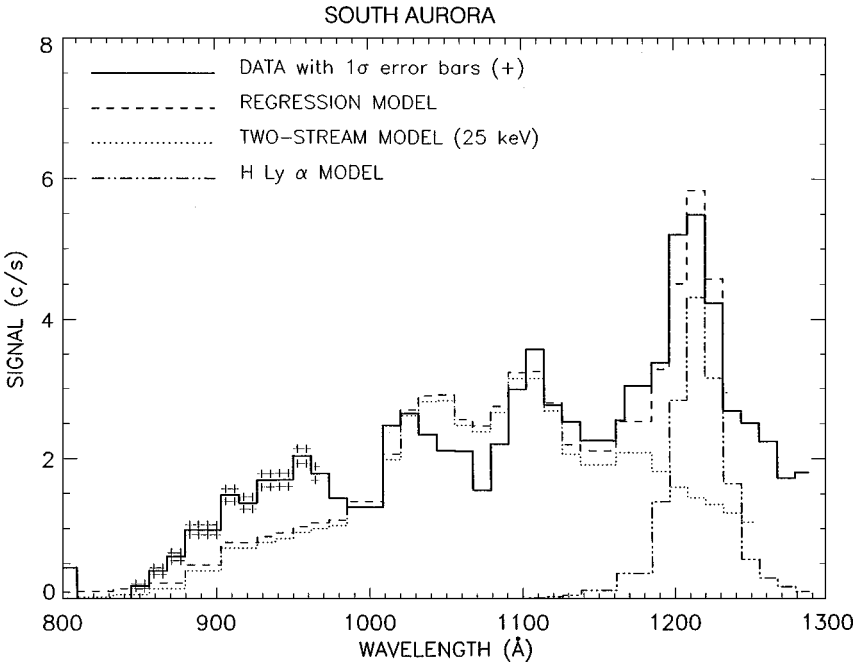

FIG. 8. The Galileo EUVS composite spectrum absolute count rate for the south aurora fitted with a 25-keV Maxwellian plus a 15-keV κ-distribution electron flux incident upon an auroral atmosphere from a two-stream code. The best fit of the data to the regression model is based upon a linear regression analysis with independent vectors of the H_2 Rydberg band and H Ly α. The 1σ error bars are shown for a portion of the Galileo spectrum. Excess EUV emission is seen between 880 and 980 Å.

H Ly α is the broad Lorentz-like interplanetary H Ly α line (see the Appendix). The way the H Ly α fills the detector array near 1215.7 Å defines a vector which serves as a surrogate to the H Ly α line in the aurora (channels 95–120 with peak signal equally divided between channels 112 and 113 on superpixel 39). Second, the two interplanetary lines at H Ly α and He 584 Å were used to define a wavelength-dependent slit function (see the Appendix). The fitting requirements are much more stringent in the present regression model than in the earlier three-layer model, since there is only one H_2 EUV Rydberg spectrum emerging from the top of the atmosphere as opposed to the three independent spectra from three layers plus H Ly α in the previous publication (Ajello *et al*. 1998). Thus, there is no fitting adjustment possible to the relative intensities to the EUV portion of the spectrum from 800–1100 Å, away from the H Ly α line.

We show in Fig. 8 and Fig. 9 the best-fit regression models to the Galileo south composite observations. The atmospheric model is the final auroral atmosphere produced by the two-stream thermal structure code. In Fig. 8 the Maxwellian component is 25 keV with the energetic EPD κ-distribution, and in Fig. 9 we use the 3-κ distribution. The best-fit models are almost identical. In fact, a total of a dozen models with characteristic energies of E_o varying from 2 to 100 keV were tried for both the north and the south. The extremes of the characteristic energies in the models include the 3-kappa distribution fit of Fig. 9, which has a strong 600-eV component to a 100-keV characteristic energy. In all the models the fit is quite good to excellent from 1000–1200 Å. However, the region from 850 to 1000 Å appears to have "excess" emission for all characteristic energies, which is unaccounted for in the model. The problem is the same for models that make use of the initial NEB polar atmosphere rather than the two-stream electron transport auroral atmosphere.

At this point, for further guidance and verification of the Galileo EUVS auroral spectral behavior, we compared the HUT UV observations of the northern aurora (P. Feldman and B. Wolven, personal communication, 2000, see also Wolven and Feldman 1998) to the Galileo EUVS observations. We show in Fig. 10 the HUT spectral data degraded to the EUVS resolution and instrument transmission function. The spectra are normalized at 1150 Å, a wavelength large enough to preclude self-absorption in the H_2 Rydberg bands. In addition, we show with similar resolution the optically thin laboratory spectrum of e + H_2 electron-impact-induced fluorescense at 100 eV (Jonin *et al*. 2000). With the same resolution the HUT spectral data displays similar relative intensities as does the Galileo spectrum from 1000 to 1200 Å. It is clear from both Fig. 8 and Fig. 9 that a low-resolution model of the HUT observations would also display excess emission from 850 to 1000 Å, although not as severe as for the Galileo EUVS. The relative intensity of the optically thin laboratory spectrum (Jonin *et al*. 2000) is dramatically different than the relative intensity of the Galileo or HUT aurora spectra. The laboratory H_2 foreground abundance was 3×10^{13} cm^{-2}. A low-resolution laboratory spectrum remains weakly affected by foreground abundances below 5×10^{13} cm^{-2}. The laboratory spectrum displays the same effect as the planetary spectra with

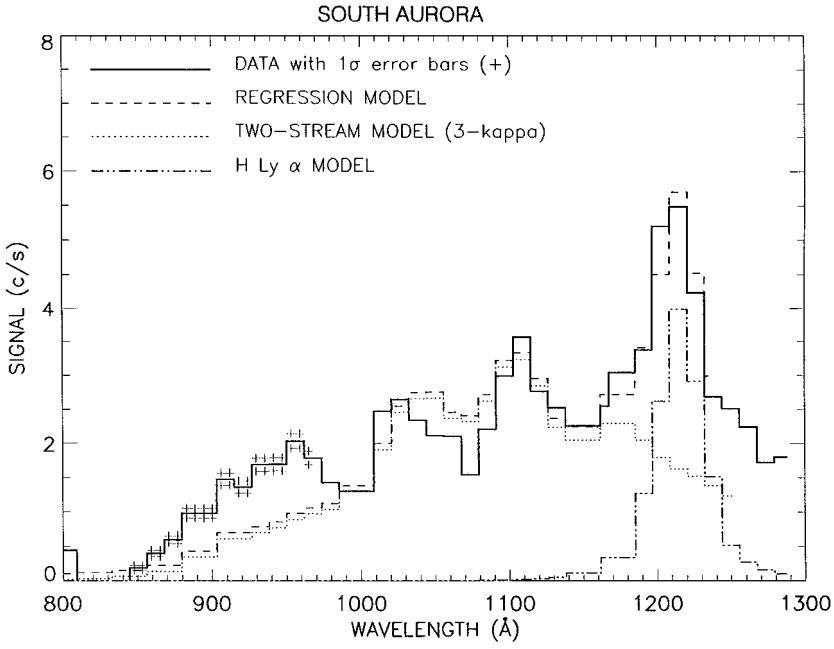

FIG. 9. The Galileo EUVS composite spectrum absolute count rate for the south aurora fitted with a 3-κ distribution electron flux incident upon an auroral atmosphere from a two-stream code. The best fit of the data to a regression model is based upon a linear regression analysis with independent vectors of the H_2 Rydberg band and H Ly α. The 1σ error bars are shown for a portion of the Galileo spectrum. Excess EUV emission is seen between 880 and 980 Å.

considerable excess emission in the EUV from 850 to 1000 Å. The effects of self-absorption in the Rydberg bands are dramatic in the Jupiter aurora. The excess auroral EUV emission is nearly optically thin and must arise high in the atmosphere.

We show the H_2 Rydberg line $v'' = 0$ resonance emission structure in Fig. 11. The line positions and intensities of Fig. 11 are based on the transition probabilities and wavelengths of Abgrall *et al*. (1994, 1999 and references therein). The

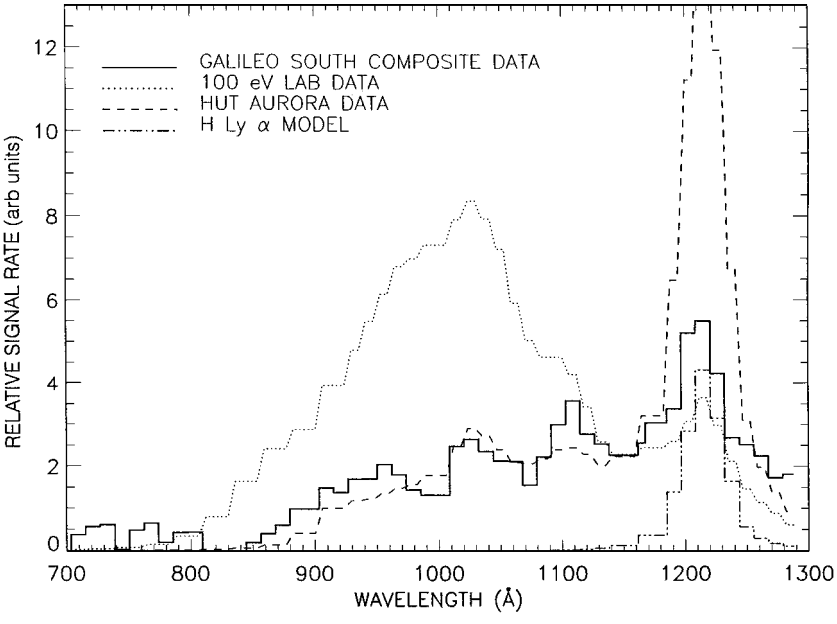

FIG. 10. The Galileo EUVS composite spectrum relative count rate for the south aurora compared to the HUT auroral EUV spectrum and a laboratory optically thin 100-eV spectrum. The HUT and laboratory spectrum have been degraded to the Galileo EUV spectral resolution of 32.6 Å FWHM with Lorentzian wings. The calibrated comparison spectra have been multiplied by the Galileo EUVS sensitivity to convert to relative count rate. The three spectra have been normalized at 1150 Å.

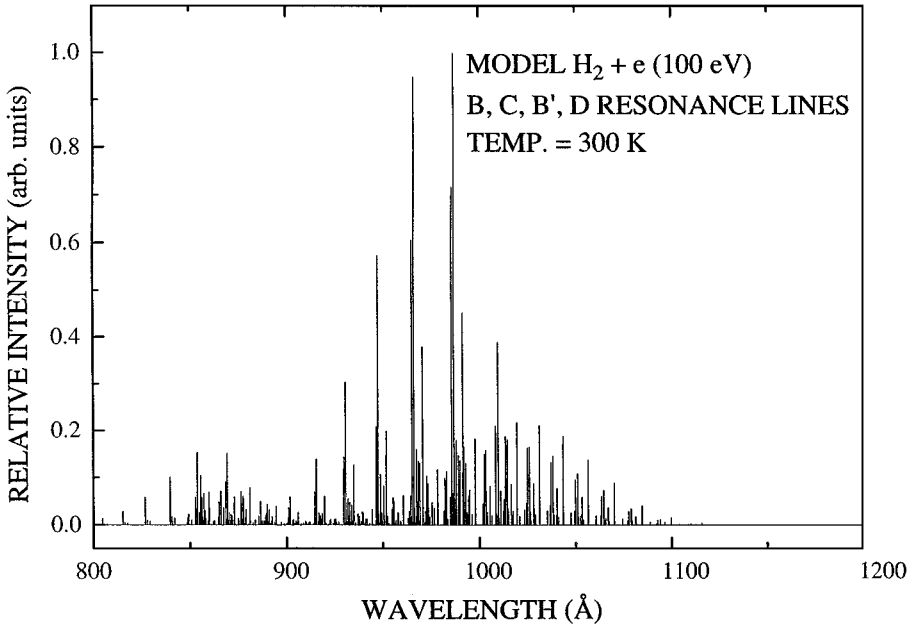

FIG. 11. Model line spectrum of the resonance bands (v′, 0) of the $B\,^1\Sigma_u^+ \rightarrow X\,^1\Sigma_g^+$, $C\,^1\Pi_u \rightarrow X\,^1\Sigma_g^+$, $B'\,^1\Sigma_u^+ \rightarrow X\,^1\Sigma_g^+$, and $D\,^1\Pi_u \rightarrow X\,^1\Sigma_g^+$ band systems at 300 K and 100 eV without self-absorption. The model is based on the line positions and transition probabilities of Abgrall *et al.* (1994, 1999) and the electron emission cross sections of Liu *et al.* (1998).

dominating Rydberg resonance structure arises from the Werner bands, whose emission cross sections peak in the 920–1020 Å range. The EUV laboratory spectrum used here has been recently discussed (Jonin *et al*. 2000, Liu *et al*. 2000).

It is more useful to study the HUT spectrum in its entirety and at full resolution. The HUT data spans both the EUV and FUV. It is a unique data set in that the FUV gives information on the characteristic energy and the EUV gives information on the location of the high-altitude aurora. We show in Fig. 12 the model regression fit to the HUT data. The best-fit model spectrum is composed of two independent auroral sources. The aurora multiple linear regression model includes H_2 bands generated by

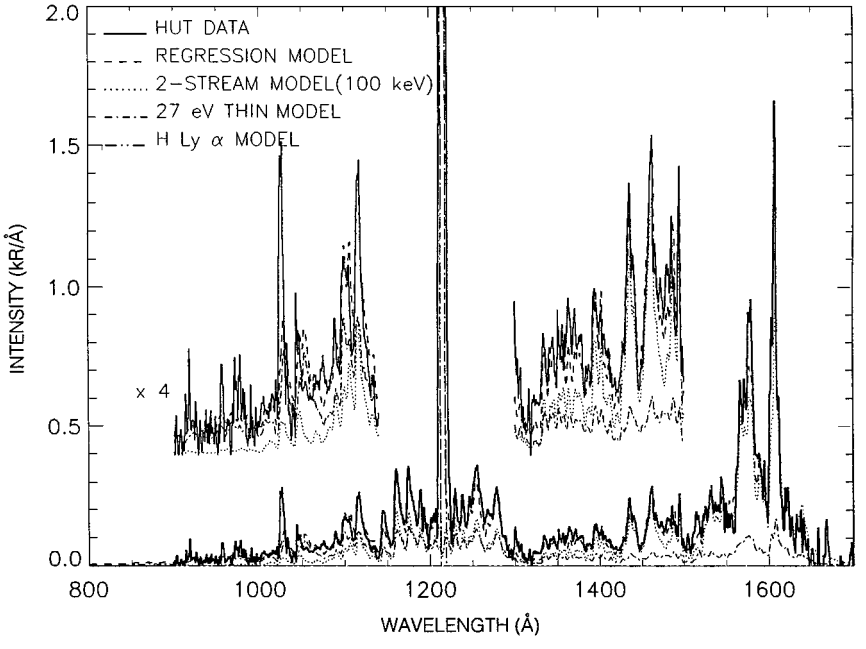

FIG. 12. The HUT UV spectrum from 850 to 1650 Å fitted with a linear regression model that includes (1) a 100-keV Maxwellian and two-stream model auroral atmosphere, (2) a 27-eV optically thin H_2 model with 3×10^{15} cm^2 foreground abundance, and (3) H Ly α.

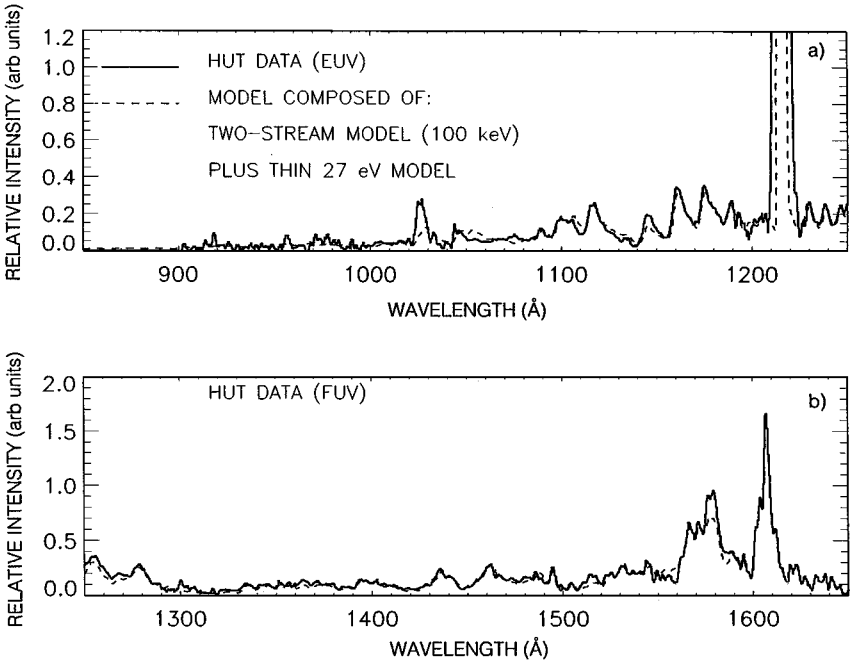

FIG. 13. (a) The HUT EUV spectrum from 850 to 1250 Å fitted with a linear regression model from Fig. 12. The HUT spectrum and EUV regression model are normalized near 1180 Å. (b) The HUT FUV spectrum from 1250 to 1650 Å fitted with a linear regression model from Fig. 12. The HUT spectrum and EUV regression model are normalized near 1610 Å.

two primary Maxwellian sources of electrons, a 100-keV deep Maxwellian aurora summed with the usual κ-function (Eq. (8)) and an optically thin 27-eV low-energy shallow aurora with foreground abundance of 3×10^{15} cm^{-2}.

The color ratio, C, of the FUV, is defined as the ratio of integrated intensities in the 'red' region to the 'blue' region of the FUV.

$$C = 4\pi I_{1556-1619\,\text{Å}}/4\pi I_{1230-1300\,\text{Å}} \tag{9}$$

is found to be 2.18 for the HUT observation compared to 1.0–1.8 for the approximately 50 Galileo north observations (Ajello *et al.* 1998) and a laboratory color ratio of 0.92 for pure H_2 gas (Liu *et al.* 1998). An extensive number (229) of IUE north auroral zone observations have been analyzed by Livengood *et al.* (1990), who found a range of color ratio variations from a bit less than 1 to slightly more than 4. The HUT observation captured a deep aurora and a strong aurora. The two-stream atmosphere requires a primary Maxwellian energy of 100 keV. Using the NEB polar model (which has more CH_4), a lower primary energy of 40 keV is required to model the HUT data to a similar degree of accuracy (0.94 correlation coefficient). The root-mean-square (RMS) fit is limited by residual Earth airglow emissions at 1025 Å and other weak airglow features found in the spectrum below 900 Å. The low-energy aurora component excited by the soft electrons is about 16% of the intensity of the total aurora as judged by comparing the intensities in the optically thin red region of the FUV spectrum, described above in the color ratio determination. The deep aurora dominates the FUV spectrum. The shallow aurora dominates the EUV spectral region for wavelengths less than 1100 Å. The two auroral components contribute roughly equal intensity from 1100 to 1300 Å. The deep aurora model employs a vibrational temperature that is twice the gas temperature to explain the enhanced self-absorption from $v'' = 1$ and 2. This effect has been observed by Wolven and Feldman (1998) and described by Cravens (1987) and Majeed *et al.* (1991). Wolven and Feldman have noted the strong effects of self-absorption near 1054 Å and 1100 Å from the C(v′, 1) and C(v′, 2) rovibronic lines, respectively. We show in Fig. 13 the EUV and FUV regions of the HUT spectrum in an expanded plot to demonstrate the quality of the fit (0.94 correlation coefficient). The two regions have been separately normalized in Fig. 13.

THE ANALYSIS OF THE GALILEO OBSERVATIONS

We now return to the Galileo north and south composite spectra described earlier. We show in Fig. 14 and Fig. 15 the regression model for the south and north composite spectra with the addition of a high-altitude layer from soft electron primary energy deposition. The high-altitude layer includes emission from both e + H and e + H_2 excitation with foreground abundances of 1×10^{15} cm^{-2} and 3×10^{15} cm^{-2}, respectively. The Galileo EUVS observation requires the addition of a small amount of emission from the high Rydberg series members of the e + H Lyman series ($n > 4$) to achieve best-fit to the excess EUV emission. The mixing ratio of H/H_2 is highly uncertain in the neighborhood of the exobase and probably highly variable

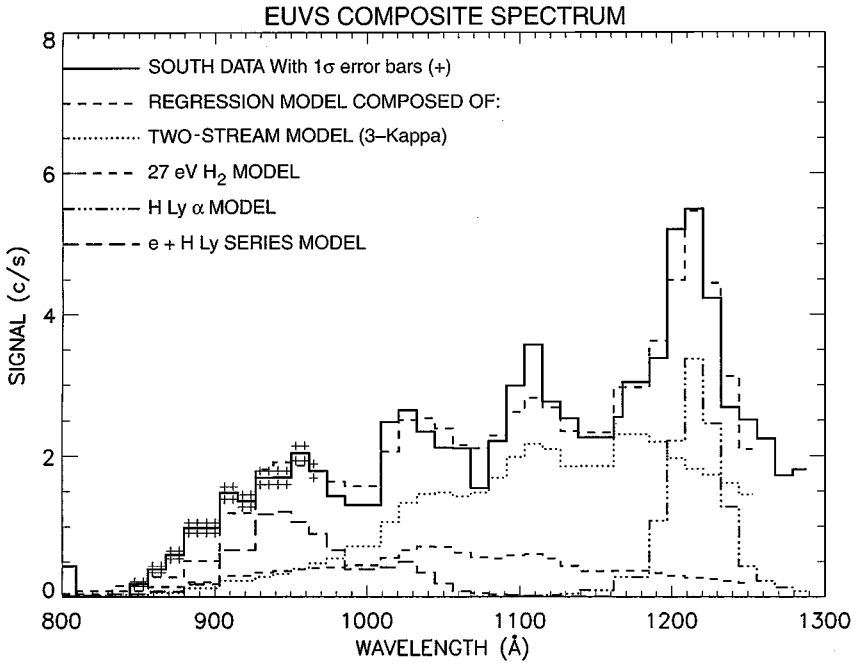

FIG. 14. The Galileo EUVS composite spectrum in units of absolute count rate for the south aurora fitted in linear regression analysis with (1) a 3-κ distribution electron flux incident upon an auroral atmosphere with an altitude-dependent secondary electron distribution and atmospheric distribution from a two-stream code, (2) a nearly optically thin H_2 Rydberg band spectrum excited by a 27-eV Maxwellian with a 3×10^{15}cm^{-2} foreground abundance in H_2, (3) an H Lyman series (n $>$ 2) from e + H excitation with 1×10^{15}cm^{-2} foreground abundance in H, and (4) H Ly α from electron impact dissociative excitation of H_2 and direct electron excitation of H. The multiple linear regression model best-fit estimation of the observational data is based upon a linear regression analysis with four independent vectors just described: (1) the H_2 Rydberg band, (2) H_2 27-eV nearly optically thin Rydberg band emission, (3) H Lyman series (n $>$ 2), and (4) H Ly α (n = 2). The 1σ error bars are shown for a portion of the Galileo spectrum.

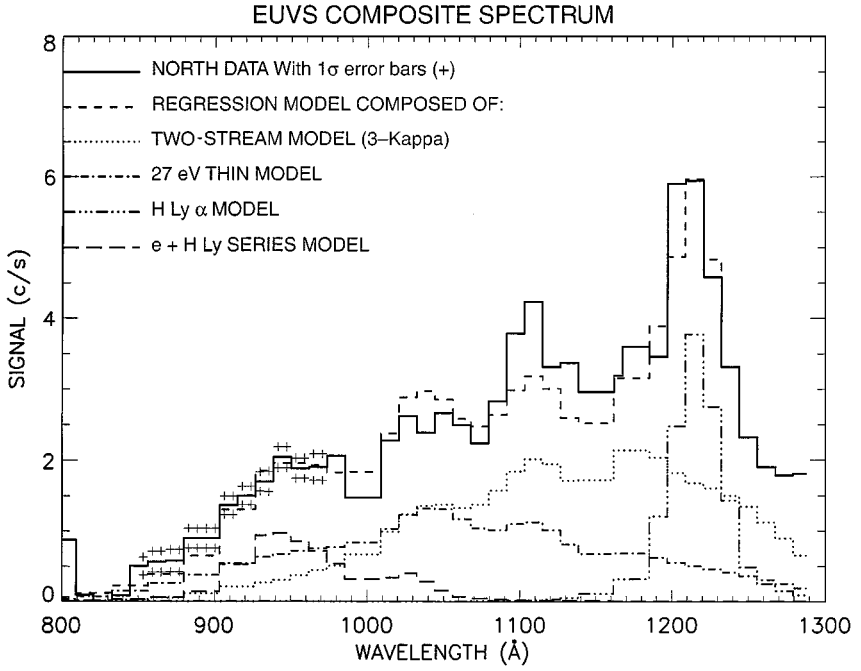

FIG. 15. The Galileo EUVS composite spectrum in units of absolute count rate for the north aurora fitted in linear regression analysis with (1) a 3-κ distribution electron flux incident upon an auroral atmosphere with an altitude-dependent secondary electron distribution and atmospheric distribution from a two-stream code, (2) a nearly optically thin H_2 Rydberg band spectrum excited by a 27-eV Maxwellian with a 3×10^{15}cm^{-2} foreground abundance, (3) an H Lyman series from e + H excitation with 1×10^{15}cm^{-2} foreground abundance, and (4) H Ly α which is modeled based on the VLISM spectrum. The regression model to the observational data is based upon a linear regression analysis with four independent vector components just described. The 1σ error bars are shown for a portion of the Galileo spectrum.

depending on the ratio of soft/hard electron fluxes. Both soft and hard electrons are very effective in dissociating H_2 to create a flux of chemically reactive H-atoms. A large soft electron energy flux, Q, could lead to winds in the upper atmosphere and affect the atomic hydrogen density on a global basis. Therefore, the distribution of atomic hydrogen near the exobase is considered a free parameter since the two-stream transport model does not include the effect of the transport of atomic hydrogen proposed here (Grodent *et al*. 2000). Additionally, the chemical models of the auroral atmosphere are not well established. The quality of the correlation coefficient is 0.98 in the south and 0.93 in the north. Figure 14 employs the 3-κ distribution in the south and Fig. 15 uses 3-κ distribution in the north. Both models use the higher vibrational temperature from the HUT models of the previous section. The energy deposition required to model the deep aurora component of the observation in Fig. 14 for the south is 87 ergs/cm^2/s. Similarly, the energy deposition required to model the deep aurora component of the observation in Fig. 15 for the north is 75 ergs/cm^2/s. The output intensity of the Rydberg bands in the south and north for the emerging spectrum is near 1.8 MR in either case for a 200-km-wide oval source. In order to fit the Galileo spectrum, the regression model requires the addition of both a deep and a shallow aurora. In a similar fashion to the HUT spectrum, the Galileo composite north and south EUV spectra present spectroscopic evidence for a high-altitude auroral component. However, fitting the Galileo EUVS spectrum requires both the e + H and the e + H_2 sources in the vicinity of the exobase. Higher primary energies up to 100 keV can be used for the characteristic energy with a similar degree of accuracy to the models. The EUV spectrum by itself is simply not capable of giving information on the characteristic energy of the deep aurora. For example, we find for 25-keV characteristic primary energy that the energy input is 61 ergs/cm^2/s for the south and 41 ergs/cm^2/s for the north with a similar energy emerging intensity to the 3-κ distribution and a similar RMS fit in each case.

DISCUSSION

We have presented spectroscopic evidence from both the Galileo EUVS and the HUT EUV + FUV observations demonstrating that there is a persistent high-altitude aurora in the vicinity of the exobase (~2000 km above the 1 bar level). This evidence supports the interpretations of the high vibrational temperatures of H_3^+ by Grodent *et al*. (2000). Grodent *et al*. found that the high exospheric temperatures of H_3^+ could be maintained by a soft electron flux. They chose to model the HST observations with an energy of 350 eV for the soft electron component. The EUV data verify their assertion and indicate that the characteristic energy is even lower, ~20–200 eV. The addition of a second strong auroral emission source high in the atmosphere serves to explain the observation of strong H_3^+ fundamental and overtone IR emissions from high temperature regions above the homopause (Kim *et al*. 1997, Drossart *et al*. 1993). It was originally assumed that all the UV emission in the main oval came from deep in the atmosphere and that the UV and IR sources were separate entities. It is clear that there is no distinct region where the UV emissions occur. Rather they are distributed throughout the thermosphere starting near the homopause with a peak at 245 km (Vasavada *et al*. 1999, Ingersoll *et al*. 1998) and attaining altitudes of the exobase, near 2000 km. Both the UV spectra and visible SSI photometric images arise from the same source process of electron excitation of H_2. A preponderance of the UV emissions results from the deep aurora, which explains the 200–800 K UV rotational temperatures in the FUV. The low-energy precipitation has as a natural result the heating of the thermosphere. This heating provides a source for the upper atmospheric thermal excess (Emerich *et al*. 1996). The turbulence created by the low-energy electron precipitation may lead to the low-latitude supersonic velocities of H-atoms as revealed by asymmetric H Ly α line profiles (Emerich *et al*. 1996, Prange *et al*. 1997).

The true measure of the characteristic energy associated with each of the different auroral regions is a model of the individual FUV spectra that spatially resolve the polar cap and the main oval. Such spectra will be forthcoming from HST STIS (Space Telescope Imaging Spectrograph) and have been obtained by HST Goddard High Resolution Spectrometer (GHRS) (Dols *et al*. 2000). It is important to point out that the composite spectra observed by Galileo EUVS and HUT and analyzed in this work are a time average and spatial average of the two principal auroral features—main oval and polar cap. Both the main oval and polar cap are present in each instrument's field of view. The high-resolution spatial and temporal dependence of auroral morphology has been clearly depicted by WFPC II and faint object camera (FOC) images described by Clarke *et al*. (1996, 1998) and Prange *et al*. (1998). It is not possible to say if the low-energy distribution is associated with only the auroral oval or the polar cap or both. Both the polar cap and auroral oval aurora GHRS spectra (Dols *et al*. 2000) have similar GHRS FUV spectra with characteristic energies of 17–40 keV and a color ratio as high as 5.5 in the polar cap. The lower energy component modeled here may be present in both the main oval and polar cap aurora.

We suggest that the electron distribution in the main auroral oval (and/or polar cap) atmosphere can be represented by at least three distinct components: (1) a low-energy tail resembling a power law from 0.01 to 0.2 keV, (2) a primary Maxwellian distribution with characteristic energy of 5–100 keV, and (3) a high-energy tail in the form of a κ-distribution as measured by EPD (Mauk *et al*. 1996, 1999) with a characteristic energy of 15 keV. This type of distribution has been discussed from a theoretical point of view by Strickland *et al*. (1993). The rise in the population of low-energy electrons below 10 eV, is described by the low-energy tail, and is shown in Fig. 4. This large population of very low-energy electrons at all altitudes is caused by the gap in energy loss processes with thresholds approximately between 4 and 10 eV. Above 11 eV, energy loss begins to increase rapidly from excitation of the large number of singlet and triplet states of H_2. The total loss function peaks near 100 eV from the large

ionization cross section of H_2 (Cravens *et al*. 1975) and thereafter continually decreases with increasing electron energy.

This analysis of the Galileo and HUT EUV spectra was the first to include detailed energy loss processes in the auroral atmosphere. The relative intensity distribution of the auroral spectrum depends on the mix of deep and shallow aurorae. Deep aurorae are characterized by an EUV relative intensity that depends chiefly on the foreground abundance of H_2. The emerging EUV spectrum is independent of depth of penetration for characteristic energies greater than 500 eV. The shallow aurora spectra are similar in relative intensity to Saturn where foreground abundances of 3×10^{15} cm^{-2} were found (Shemansky 1985, Shemansky and Ajello 1983). The Voyager Saturn spectra also show a sharp peak at 920 Å characteristic of e + H Lyman series excitation. A similar excess emission at 920 Å was found in the Galileo Jupiter observations. The high order Lyman series Rydberg transitions are stronger than even the H Ly β emission because they remain optically thin at the foreground column densities ($\sim 10^{15}$ cm^{-2}) present near the exobase.

The importance in accurately knowing the slit filling factor of the emissions in analyzing the Galileo and HUT sets of EUV data is illustrated with the factor of 10 difference in the energy input to the atmosphere. The pixel spatial resolution of WFPC II on the surface of Jupiter is about 380 km. The primary arc oval width of 170–460 km measured by Galileo on G7 would suggest a smaller fill-factor than the HUT estimate (3.7×10^{-11} sr for a 200-km-wide source [Vasavada *et al*. 1999]). On orbit C3, an SSI photograph also indicated an auroral arc FWHM of 270 km in the same range as G7 (Ingersoll *et al*. 1998). However, another SSI image on C3 indicated a wider auroral oval $\sim$1000 km FWHM. The WFPC II image (Morrissey *et al*. 1997) shows an irregular emitting region of varying width, and portions of the oval are narrow and unresolved. The emission is very broad where it is very intense. This region fills about half the pixels. On the other hand, using the SSI observation which shows the width of the dawn terminator region as being approximately 200 km yields an average energy input of $\sim$40–80 ergs/cm^2/s. Thus the HUT observations would have yielded a similar energy output to that of Galileo had we used the G7 size criterion for the oval. The WFPC II picture, which is simultaneous with the HUT spectral observations, yields a 10 times broader aurora with an average energy input of $\sim$4 ergs/cm^2/s. This energy flux is also in contradistinction to the Galileo G7 analysis (Pryor *et al*. 2000), which finds a Q_o of 425 ergs/cm^2/s. We do however agree with one of the primary HUT results that the vibrational temperature is elevated with respect to the kinetic temperature (Wolven and Feldman 1998). The mechanisms for the production of vibrationally excited H_2 have been discussed by Cravens (1987). Radiative loss by vibrational–rotational transitions is dipole-forbidden. Hence important chemistry is initiated by vibrationally excited H_2 reactions with H, H_2, and H^+.

The PLS measurements (Frank and Patterson 2000) of field-aligned electron beams in the equatorial middle magnetosphere would support a large energy flux of 100 ergs/cm^2/s or greater conveyed by electrons of 0.1–2 keV, whereas the corresponding high-energy EPD measurements (Williams *et al*. 1999) of field-aligned electron beams find a much lower energy flux of $\sim$15 ergs/cm^2/s for $E_o > 15$ keV in the vicinity of Io. Based on this variation in the middle magnetosphere the low-energy electron distribution below 15 keV in the 20–30 R_j region may be very important in exciting the aurora. This energy region from 2 to 15 keV in the Galileo fields and particles database should be a very important region for increasing our understanding of the aurora. The energy flux measured by PLS above 10 keV is very small and of the same order of flux intensity as EPD indicates in the middle magnetosphere near the orbital plane of the satellites. The flux requirements for the 25-keV deep aurora location at 245 km as measured by the combined SSI and UVS/HUT results can be reconciled by field-aligned potentials in the inner magnetosphere. The down-going primary electron beam flux may be accelerated in the region of 1 R_j by analogy to that on the Earth (Akasofu 1991). The upward field-aligned current is the process that produces the strong FUV emissions. The Earth's aurora has similar acceleration processes (Mauk and Meng 1991). Upward-going electrons (downward current) may contribute to the optically thin EUV emissions in either or both the main oval and polar cap auroral regions. The upward-going electrons are associated with the 'black aurora' on Earth (Carlson *et al*. 1998). The acceleration process, if present, probably begins near the exobase at the top-side of the ionosphere. Although energy deposition on the Earth can attain 10–100 ergs/cm^2, the emissions on Jupiter tend to be 100–1000 times more intense (1 MR on Jupiter compared to 10 kR on Earth). Alternatively, the aurora may be temporally variable and spatially patchy and may repetitively switch from the high-energy particle beams to the steady drain of hot isotropic plasma sheet ions and electrons from the middle magnetosphere. The observations presented herein are an average over sufficiently long time scales, compared to aurora temporal variability, so as to represent an average over both types of aurorae. Another important point from this analysis is that the color ratio measured in the FUV by a UV spectrometer is an average of the spectra from both soft and hard electron aurorae. Figure 12 indicates that approximately half of the blue interval (1230–1300 Å) HUT integrated intensity in Eq. (9) can be attributed to the soft electron component. Based on the model, the color ratio prediction would be close to 4 for an observation of the hard component by itself. The primary high-energy electron beam would reach column density levels of approximately 2×10^{17} cm^2 in CH_4 corresponding to an altitude of about 200 km (above the 1 bar level in Fig. 7) to account for this color ratio. On the other extreme, clearly spectra were observed by Galileo that were unaffected by hydrocarbon absorption (minimum FUV sensitivity in CH_4 of 1×10^{16} cm^2) corresponding to penetration altitudes above 250 km (Ajello *et al*. 1998). These spectra from shallow aurora were entirely generated by low-energy electrons stopped above the homopause.

Based on modeling the HUT spectra, the deposition of 1–10 ergs/cm^2/s of heat energy into an atmospheric region of low

specific heat capacity near the exobase by the soft electrons needs to be modeled to understand the changes in the thermal structure and global dynamics. SSI has searched for the high-altitude emissions from acquired images with no success (Vasavada, personal communication, 2000). Pryor *et al*. (2001) have pointed out that the visible emissions are generally smaller than the FUV emissions by a factor of approximately 50, rendering them difficult to observe. The next important step to better understand the brighter (in the FUV) and deeper aurora from the hard electron distribution is to synthesize the complementary databases of Galileo EPD and PLS to cover the entire electron energy range from 1 eV to 1 MeV. A unified electron distribution function can be used to model the acceleration processes in the inner magnetosphere.

APPENDIX: EUVS TRANSMISSION FUNCTION

The observation of the VLISM by the Galileo EUVS for over 10^6 s during the Earth One encounter observation period in 1990 offered an opportunity to provide an in-flight calibration of the instrument transmission function. We show in Fig. 16 the long-term measurement and model of the interplanetary glow at the multiplet lines He(584.2 Å) and H(1025.7, 1215.7 Å) with a small amount of diffuse scattered star light. The signal in H Ly α amounted to over 3×10^6 counts. The transmission function has a trapezoidal core of 32.6 Å FWHM and a peak HM of 0.2 Å. The underlying broad exponential wings are wavelength dependent. The FWHM of the wings are wavelength dependent varying from 96 Å at H Ly α to 44 Å at He 584 Å. Based on the peak to peak separation of H Ly α to He 584 Å the instrument dispersion was reduced by 0.6% from the preflight value (Hord *et al*. 1992) from 5.91 to 5.87 Å/ch. The H_2 model of Rydberg lines were convolved with the VLISM-based EUVS transmission function and the preflight calibration (sensitivity in c/s/kR) to give the model count rate for the 126 active pixels. The EUVS was programmed to use 44 superpixels in the Galileo low gain mission (Ajello *et al*. 1998). Photon counts were divided equally among the 2–4 channels composing the superpixel element.

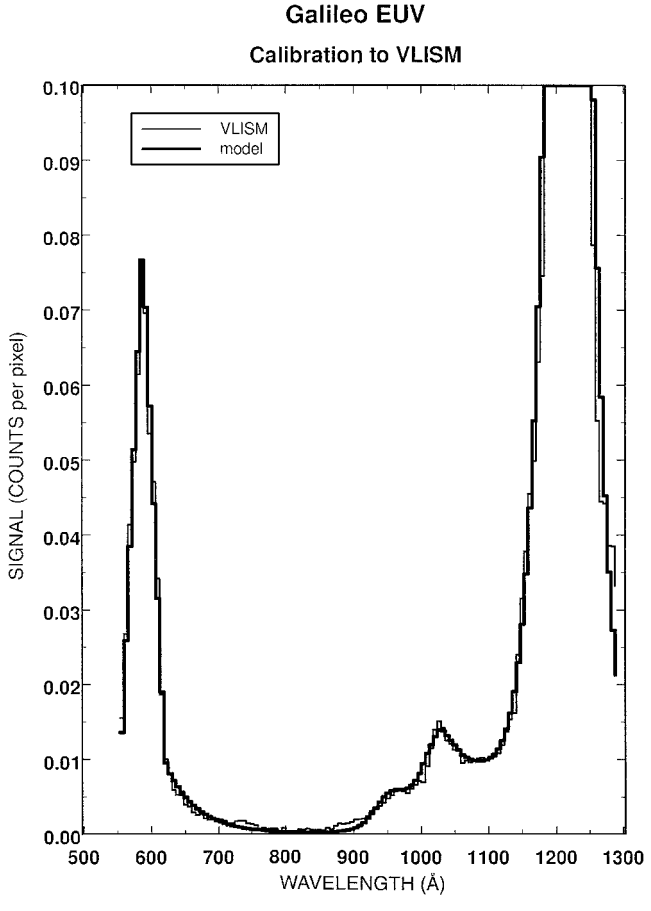

FIG. 16. The Galileo EUVS line transmission function (counts per pixel) based upon observations of the interplanetary H Ly α and He (584 Å) glow. The VLISM spectrum is modeled by including emissions from H Ly α, H Ly β, and the diffuse interstellar background.

ACKNOWLEDGMENTS

The research described in this text was carried out at the Jet Propulsion Laboratory, California Institute of Technology, the University of Colorado, the University of Southern California, the Southwest Research Institute, and the University of Liege. The work was supported by the NASA Jupiter Science Data Analysis Program, the Galileo Project, the Air Force Office of Scientific Research (AFOSR), and the NASA Planetary Atmospheres Program Office. We gratefully acknowledge receipt of the HUT data from P. Feldman and B. Wolven. We have benefited from discussions with J. Clarke, B. Tsurutani, D. Williams, L. Frank, B. Wolven, P. Feldman, W. Peterson, and Y. Yung.

REFERENCES

Abgrall, H., E. Roueff, F. Launay, and J.-Y. Roncin 1994. The $B'\,^1\Sigma_u^+ \rightarrow X\,^1\Sigma_g^+$ and $D\,^1\Pi_u \rightarrow X\,^1\Sigma_g^+$ band systems of molecular hydrogen. *Can. J. Phys.* **72**, 856–865.

Abgrall, H., E. Roueff, I. Drira 1999. Total transition probability and spontaneous radiative dissociation of B, C, B′, and D states of molecular hydrogen. *Astron. Astrophys. Supp.* **141**, 297–300.

Ajello, J. M., D. E. Shemansky, T. L. Kwok, and Y. L. Yung 1984. Studies of extreme ultraviolet emission from Rydberg series of H_2. *Phys. Rev. A* **29**, 636–653.

Ajello, J. M., and 11 colleagues 1988. A simple ultraviolet calibration source with reference spectra and its use with to the Galileo orbiter ultraviolet spectrometer. *Appl. Opt.* **27**, 890–914.

Ajello, J. M., and 13 colleagues 1998. Galileo orbiter ultraviolet spectra of Jupiter. *J. Geophys. Res.* **103**, 20,125–20,148.

Akasofu, S. I. 1991. Auroral phenomena. In *Auroral Physics* (C.-I. Meng, M. J. Rycroft, and L. A. Frank, Eds.), pp. 223–239. Cambridge Univ. Press, New York.

Bhardwaj, A., and G. R. Gladstone 2000. Auroral emissions of the giant planets. *Rev. Geophys.* **38**, 295–353.

Carlson, C. W., and 13 colleagues 1998. FAST observations in the downward auroral region: Energetic upgoing electron beams, parallel potential drops, and ion heating. *Geophys. Res. Lett.* **25**, 2017–2020.

Clarke, J. T., and 20 colleagues 1996. Far ultraviolet imaging of Jupiter's aurora and the Io "footprint." *Science* **274**, 404–408.

Clarke, J. T., and 10 colleagues 1998. Hubble Space Telescope imaging of Jupiter's UV aurora during the Galileo orbiter mission. *J. Geophys. Res.* **103**, 20,217–20,236.

Cravens, T. E., G. A. Victor, and A. Dalgarno 1975. The absorption of energetic electrons by molecular hydrogen gas. *Planet. Space Sci.* **23**, 1059–1070.

Cravens, T. E. 1987. Vibrationally excited molecular hydrogen in the upper atmosphere of Jupiter. *J. Geophys. Res.* **92**, 11,083–11,100.

Dols, V., J. C. Gerard, J. T. Clarke, J. Gustin, and D. Grodent 2000. Diagnostics of the Jovian aurora deduced from ultraviolet spectroscopy: Model and GHRS observations. *Icarus* **147**, 251–266.

Drossart, P., B. Bezard, S. Atreya, J. Bishop, J. H. Waite, and D. Boice 1993. Thermal profiles in the auroral region. *J. Geophys. Res.* **98**, 18,803–18,811.

Dziczek, D., J. Ajello, G. James, D. L. Hansen 2000. A study of the cascade contribution to the H_2 Lyman band system from electron impact. *Phys. Rev. A* **61**, 64,702-1–64,702-4.

Emerich, C., L. B. Jaffel, J. T. Clarke, R. Prange, G. R. Gladstone, J. Sommeria, and G. Ballester 1996. Evidence for supersonic turbulence in the upper atmosphere of Jupiter. *Science* **273**, 1085–1087.

Frank, L. A., and W. R. Patterson 2000. Observations of plasmas in the Io torus with the Galileo spacecraft. *J. Geophys. Res.* **105**, 16,017–16,034.

Gerard, J.-C., and V. Singh 1982. A model of energy deposition of energetic electrons and EUV emissions in the jovian and saturnian atmospheres and implications. *J. Geophys. Res.* **87**, 4525–4532.

Gladstone, G. R., M. Allen, and Y. L. Yung 1996. Hydrocarbon photochemistry in the upper atmosphere of Jupiter. *Icarus* **119**, 1–52.

Gladstone, G. R., and T. E. Skinner 1989. Spectral analysis of jovian auroral emissions. In *Time Variable Phenomena in the Jovian System* (M. J. Belton, R. A. West, and J. Rahe, Eds.), pp. 221–228. Spec. Publ. SP-494, NASA Washington, DC.

Grodent, D., J. H. Waite, and J. C. Gerard 2000. A self-consistent model of the jovian thermal auroral thermal structure. *J. Geophys. Res*, in press.

Herbert, F., B. R. Sandel, and A. L. Broadfoot 1987. Observations of the jovian UV aurora by Voyager. *J. Geophys. Res.* **92**, 3141–3154.

Hord, C. W., and 12 colleagues 1992. Galileo ultraviolet spectrometer experiment. *Space Sci. Rev.* **60**, 503–530.

Ingersoll, A.P., A. R. Vasavada, B. Little, C. D. Anger, S. J. Bolton, C. Alexander, K. P. Klaasen, W. K. Tobiska, and the Galileo SSI Team 1998. Imaging Jupiter's aurora at visible wavelengths. *Icarus* **135**, 251–264.

James, G. K., J. M. Ajello, and W. R. Pryor 1998. The middle ultraviolet-visible spectrum of H_2 excited by electron impact. *J. Geophys. Res.* **103**, 20,113–20,123.

Jonin, C., X. Liu, J. M. Ajello, G. K. James, and H. Abgrall 2000. High-resolution electron impact spectrum of H_2: I Cross sections and predissociation yields. *Astrophys. J. Supp.* **129**, 247–266.

Kim, Y. H., J. J. Caldwell, and J. L. Fox 1995. High-resolution ultraviolet spectroscopy of Jupiter's aurora with the Hubble Space Telescope. *Astrophys. J.* **447**, 906–914.

Kim, Y. H., J. L. Fox, and J. J. Caldwell 1997. Temperatures and altitudes of Jupiter's ultraviolet aurora inferred from GHRS observations with the Hubble Space Telescope. *Icarus* **128**, 189–201.

Kim, S. J., D. H. Lee, and Y. H. Kim 1998. Jovian aurorae. *Rep. Prog. Phys.* **61**, 525–568.

Kruk, J. W., S. T. Durrance, G. A. Kriss, A. F. Davidsen, W. P. Blair, B. R. Epsey, and D. S. Finley 1995. Performance and preliminary calibration of the Hopkins Ultraviolet Telescope on the Astro-2 Mission. *Astrophys. J.* **454**, L1–L6.

Lam, H. A., N. Achilleos, S. Miller, J. Tennyson, L. Trafton, T. R. Geballe, and G. Ballester 1997. A baseline spectroscopic study of the infrared auroras of Jupiter. *Icarus* **127**, 379–383.

Liu, W., and A. Dalgarno 1996. The ultraviolet spectra of the jovian aurora. *Astrophys. J.* **467**, 446–453.

Liu, X., D. E. Shemansky, S. M. Ahmed, G. K. James, and J. M. Ajello 1998. Electron impact cross sections of the Lyman and Werner band systems of hydrogen. *J. Geophys. Res.* **103**, 26,739–26,758.

Liu, X., D. E. Shemansky, J. M. Ajello, C. Jonin, G. K. James, and H. Abgrall 2000. High-resolution electron impact spectrum of H_2: II 760–900 Å. *Astrophys. J. Supp.* **129**, 267–280.

Livengood, T. A., D. F. Strobel, and H. W. Moos 1990. Long-term study of longitudinal dependence in primary particle precipitation in the north jovian aurora. *J. Geophys. Res.* **95**, 10,375–10,388.

Majeed, T., J. C. McConnell, and R. V. Yelle 1991. Vibrationally excited H_2 in the outer planets thermosphere: Fluorescence in the Lyman and Werner bands. *Planet. Space Sci.* **33**, 1591–1606.

Mauk, B. H., S. A. Gary, M. Kane, E. P. Keath, S. M. Krimigis, and T. P. Armstrong 1996. Hot plasma parameters of Jupiter's magnetosphere. *J. Geophys. Res.* **101**, 7685–7695.

Mauk, B. H., D. J. Williams, R. W. McEntire, K. K. Khurana, and J. G. Roederer 1999. Storm-like dynamics of Jupiter's inner and middle magnetosphere. *J. Geophys. Res.* **104**, 22,759–22,778.

Mauk, B. H., and C.-I. Meng 1991. The aurora and middle magnetosphere processes. In *Auroral Physics* (C.-I. Meng, M. J. Rycroft, and L. A. Frank, Eds.), pp. 223–239. Cambridge Univ. Press, New York.

Morrissey, P. F., P. D. Feldman, J. T. Clarke, B. C. Wolven, D. F. Strobel, S. T. Durrance, and J. T. Trauger 1997. Simultaneous spectroscopy and imaging of the jovian aurora with the Hopkins Ultraviolet Telescope and with the Hubble Space Telescope. *Astrophys. J.* **476**, 918–923.

Newell, P. T., C.-I. Meng, and D. A. Hardy 1991. Overview of electron and ion precipitation in the Auroral Oval. In *Auroral Physics* (C.-I. Meng, M. J. Rycroft, and L. A. Frank, Eds.), pp. 85–93. Cambridge Univ. Press, New York.

Perry, J. J., Y. H. Kim, J. L. Fox, and H. S. Porter 1999. Chemistry of the jovian auroral ionosphere. *J. Geophys. Res.* **104**, 16,541–16,565.

Prange, R., D. Rego, L. Pallier, L. B. Jaffel, C. Emerich, J. Ajello, J. T. Clarke, and G. Ballester 1997. Self-reversed Lyman-α lines from the jovian aurorae with the Hubble Space Telescope. *Astrophys. J.* **484**, L169–L173.

Prange, R., D. Rego, L. Pallier, J. E. P. Connerny, P. Zarka, and J. Queinned 1998. Detailed study of FUV jovian aurora features with the post-COSTAR HST faint object camera. *J. Geophys. Res.* **103**, 20,195–20,215.

Pryor, W. R., and 12 colleagues 1998. Galileo ultraviolet spectrometer observations of Jupiter's auroral spectrum from 1600–3200 Å. *J. Geophys. Res.* **103**, 20, 149–20,158.

Pryor, W. R., and 13 colleagues. Jupiter's ultraviolet aurora on Galileo Orbit G7. *Icarus*, submitted.

Satoh, T., J. E. P. Connerney, and R. L. Baron 1996. Emission source model of Jupiter H_3^+ Aurorae: A generalized inverse analysis of images. *Icarus* **122**, 1–23.

Seiff, A., and 9 colleagues 1998. Thermal structure of Jupiter's atmosphere near the edge of a 5-μm hotspot in the north equatorial belt. *J. Geophys. Res.* **103**, 22,857–22,889.

Shemansky, D. E., and J. M. Ajello 1983. The Saturn spectrum in the EUV—electron-excited hydrogen. *J. Geophys. Res.* **88**, 459–464.

Shemansky, D. E. 1985. An explanation for the H Ly α longitudinal asymmetry in the equatorial spectrum of Jupiter: An outcorp of paradoxical energy deposition in the exosphere. *J. Geophys. Res.* **90**, 2673–2694.

Shemansky, D. E., J. M. Ajello, and D. T. Hall 1985. Electron impact excitation of H_2: Rydberg band systems and the benchmark cross section for H Lyman α. *Astrophys. J.* **296**, 765–773.

Strickland, D. J., R. E. Daniell, J. R. Jasperse, and B. Basu 1993. Transport-theoretic model for the electron–proton hydrogen aurora, 2. Model results. *J. Geophys. Res.* **98**, 21,533–21,548.

Trafton, L. M., J.-C. Gerard, G. Munhoven, and J. H. Waite 1994. High-resolution spectra of Jupiter's northern auroral emission with the Hubble Space Telescope. *Astrophys. J.* **421**, 816–827.

Trafton, L. M., V. Dols, J.-C. Gerard, J. H. Waite, G. R. Gladstone, and G. Munhoven 1998. HST spectra of the jovian ultraviolet aurora: Search for heavy ion precipitation. *Astrophys. J.* **507**, 955–967.

Tsurutani, B. T., and 13 colleagues 1997. Plasma wave characteristics of the jovian magnetopause boundary layer: Relationship to the jovian aurora? *J. Geophys. Res.* **102**, 4751–4764.

Vasavada, A. R., A. H. Bouchez, A. P. Ingersoll, B. Little, and C. D. Anger 1999. Jupiter's visible aurora and Io footprint. *J. Geophys. Res.* **104**, 20,133–27,142.

Waite, J. H., T. E. Cravens, J. Kozyra, A. F. Nagy, S. K. Atreya, and R. H. Chen 1983. Electron precipitation and related aeronomy of the jovian thermosphere and ionosphere. *J Geophys. Res.* **88**, 6143–6163.

Waite, J. H., J. T. Clarke, T. E. Cravens, and C. M. Hammond 1988. The jovian aurora: Electron or ion precipitation? *J. Geophys. Res.* **93**, 7244–7250.

Williams, D. J., R. M. Thorne, and B. Mauk 1999. Energetic electron beams and trapped electrons at Io. *J. Geophys. Res.* **104**, 14,739–14,753.

Wolven, B. C., and P. D. Feldman 1998. Self-absorption by vibrationally excited H_2 in the Astro-2 Hopkins Ultraviolet Telescope spectrum of the jovian aurora. *Geophys. Res. Lett.* **25**, 1537–1540.